# Design, Fabrication, and Testing of Double Negative Metamaterials

*Richard W. Ziolkowski*
Department of Electrical and Computer Engineering
University of Arizona
1230 E. Speedway Blvd.
Tucson, AZ 85721-0104

**ABSTRACT:** The design, fabrication, and testing of several metamaterials that exhibit double negative (DNG) medium properties at X-band frequencies are reported. Double negative media are materials in which the permittivity and permeability are both negative. Simulation and experimental results are given that demonstrate the realization of DNG metamaterials matched to free-space. The extraction of the effective permittivity and permeability for these metamaterials from reflection and transmission data at normal incidence is treated. It is shown that the metamaterials studied exhibit DNG properties in the frequency range of interest.

# I. Introduction

Several recent papers have exposed the usefulness of metamaterials that produce negative indexes of refraction [1] - [8]. Metamaterials (MTMs) denote artificially constructed materials having electromagnetic properties not generally found in nature. Examples include photonic band gap structures [2], [9] and double negative (DNG) media [1], [3]-[8], i.e., MTMs having negative permittivity and negative permeability. Pendry [3] has proposed the possibility that a DNG medium with a negative index of refraction might overcome known problems with common lenses to achieve a "perfect" lens, which would focus the entire spectrum, both the propagating as well as the evanescent spectra. Pendry's analysis followed much of the original work of Veselago [1]. Ziolkowski and Heyman [10] have elucidated the physics of wave propagation in DNG media and have shown that such a "perfect" lens is not realizable with any realistic MTM construct. On the other hand, they demonstrated that waves in general DNG media focus in a paraxial sense along the propagation axis, i.e., they coalesce into localized beam fields that channel the power flow. The DNG slab can thus act like a convertor from a pulsed cylindrical or spherical wave to a pulsed beam.

Having indicators of the potential theoretical importance of DNG media, it becomes very desirable to design and fabricate MTMs that can achieve these properties. Several MTMs comprised of a substrate with embedded capacitively loaded strips (CLSs) and split ring resonators (SRRs) are considered here. These materials were designed with both ANSOFT's High Frequency Structure Simulator (HFSS) tools and finite difference time domain (FDTD) simulators. A variety of reflection ($S_{11}$) and transmission ($S_{21}$) results are given for the scattering of normally incident plane waves from MTM slabs that *can be interpreted* in terms of these slabs having effective negative permittivities and permeabilities. In particular, MTMs that exhibit DNG material properties matched to free-space are emphasized.

Two cases of MTMs, one in which the inclusions are non-planar and one in which they are planar, that were fabricated and then tested at normal incidence in the X-Band frequency regime are reported. Very good agreement between the simulation and experimental values of the S-parameters is demonstrated. Inversion formulas that allow the extraction of the effective permittivities and permeabilities from these MTM S-parameter results are then presented. Note that these MTM effective permittivities and permeabilities are derived to complement and to help explain and interpret the more rigorous HFSS and FDTD simulations and the experimental results. This extraction approach is applied first to a third MTM case that for normal incidence exhibits simplified transmission and reflection responses. This simplified MTM case is used to understand better what the effective permittivity and permeability results mean. The extraction formulas are then applied to the more complicated planar MTM case. Combining the S-parameter comparisons and the extraction procudure results, it is demonstrated that DNG MTMs have been designed and fabricated and

exhibit the properties predicted by the HFSS and FDTD simulations.

## II. Double negative media

The initial design of a DNG medium began with the concept of treating the electric and magnetic properties separately. In particular, the artificial material concepts reported in [11]-[18] were used. The first MTM case thus considered was the non-planar inclusion configuration shown in Fig. 1. It was expected that the capacitively-loaded strips (CLSs) would produce strong dielectric-like responses. These inclusions (half of a Jerusalem cross) have been used previously in frequency selective surface and artificial dielectric applications (see, for instance, [19]-[28]). Similarly, it was expected that the split ring resonators (SRRs) (a square version of the SRRs reported, for example, in [4], [5]) would produce strong magnetic material-like responses. The split ring resonantor (SRR) structures considered here consisted of two concentric square rings, each with gaps, and the gaps appearing on opposite sides. The non-planar concept was selected to isolate these inclusions and, hence, their electric and magnetic material properties as much as possible.

According to the analyses discussed in [11]-[18], the CLS should provide a dielectric susceptibility response associated with a "lossless" electrically small dipole of capacitance C and length $l_0$ loaded with inductance $L$ in an effective volume $V$. With the time dependence $\exp(j\omega t)$ a Thévenin circuit model of the antenna and load yields the electric susceptibility

$$\chi_e = \frac{K_e}{j\omega[j\omega L + j/(\omega C)]} = \frac{K_e}{L}\left(\frac{1}{-\omega^2+\omega_0^2}\right) \tag{1}$$

where for normal incidence $K_e = l_0^2/(\varepsilon_0 V)$ and the resonant angular frequency $\omega_0 = 1/\sqrt{LC}$. Thus the CLS should produce a "lossless" Lorentz material (LM) type of behavior near $f_0 = \omega_0/2\pi$. Similarly, the SRRs should produce a magnetic susceptibility associated with a "lossless" electrically small loop of area $A$ and inductance $L$ loaded with capacitance $C$ in an effective volume $V$. With the time dependence $\exp(j\omega t)$, a Thévenin circuit model of the antenna and load yields the magnetic susceptibility:

$$\chi_m = \frac{-j\omega K_h}{j\omega L + j/(\omega C)} = \frac{K_h}{L}\left(\frac{+\omega^2}{-\omega^2+\omega_0^2}\right) \tag{2}$$

where for normal incidence $K_h = \mu_0 A^2/V$ and again the resonant angular frequency $\omega_0 = 1/\sqrt{LC}$. Thus the SRR should produce a "lossless" Two-Time Derivative Lorentz material (2TDLM) type of behavior near

$f_0 = \omega_0/2\pi$. In particular, a magnetic 2TDLM is described by its magnetization field behavior in the time and frequency domains as

$$\partial_t^2 M + \gamma \partial_t M + \omega_0^2 M = \left[\omega_p^2 \chi_\alpha H + \omega_p \chi_\beta \partial_t H + \chi_\gamma \partial_t^2\right] H \tag{3}$$

$$\chi_m = \frac{M(\omega)}{H(\omega)} = \frac{\omega_p^2 \chi_\alpha + j\,\omega\omega_p \chi_\beta - \omega^2 \chi_\gamma}{-\omega^2 + j\,\gamma\omega + \omega_0^2} \tag{4}$$

The result (2) is recovered with $\gamma = \chi_\alpha = \chi_\beta = 0$ and $\chi_\gamma = -1$. The 2TDLM model reduces to the Lorentz model when $\chi_\beta = \chi_\gamma = 0$. A plasma frequency $\omega_p$ is introduced to make the material constants $\chi_\alpha, \chi_\beta, \chi_\gamma$ unitless. Note that as $\omega \to \infty$, the SRR's gap acts like a short and should produce a negative susceptibility [22] which agrees with Eq. (4). The result (2) agrees with the analysis of the SRRs given in [4]. Equations (1) and (2) indicate that one can potentially realize relative negative permittivities $\varepsilon_r = \varepsilon/\varepsilon_0 = (1 + \chi_e)$ and permeabilities $\mu_r = \mu/\mu_0 = (1 + \chi_m)$ just beyond the resonant frequency $f_0$ with these types of inclusions.

We note that the use of inclusions to achieve negative permittivity materials was used early in the 1960's, e.g. see [27], to simulate plasma media whose susceptibilities are given in the form of (1) with $\omega_0 \to 0$. The resulting electric susceptibility takes the lossy Drude model form and the plasma permittivity becomes:

$$\varepsilon = \varepsilon_0 \left[1 - \frac{\omega_p^2}{\omega\,(\omega - j\,\gamma)}\right] \tag{5}$$

This relation indicates that the permittivity will become negative at frequencies below the plasma frequency $\omega_p$; hence, the resulting medium will become reflective there. Thus, the interpretation of the reflection properties of a FSS as resulting from a medium with an effective permittivity that is negative at the reflection frequency has been proposed and used in FSS design. A similar thought process was used in [16] to achieve an effective 2TDLM magnetic reflector.

If the negative permittivity and permeability values can be matched over a range of frequencies, the reflection coefficient of the slab is zero. In particular, recall that in free space the wave impedance is given by $\eta_0 = \sqrt{\mu_0/\varepsilon_0}$, where the free-space permittivity and permeability are, respectively, $\varepsilon_0$ and $\mu_0$. Consider a semi-infinite medium with permittivity $\varepsilon$ and permeability $\mu$. At the interface between the slab and free-space, the reflection coefficient for normal incidence has the well-known form:

$$\Gamma = \frac{\sqrt{\mu_r/\varepsilon_r} - 1}{\sqrt{\mu_r/\varepsilon_r} + 1} = \frac{\eta - 1}{\eta + 1} \tag{6}$$

where the relative impedance $\eta = \sqrt{\mu_r/\varepsilon_r}$. For a slab of finite thickness $d$ of this medium, the reflection and transmission coefficients for plane wave scattering at normal incidence are given, respectively, by the S-parameters $S_{11}$ and $S_{21}$:

$$S_{11} = \frac{(\eta^2-1)(1-Z^2)}{(\eta+1)^2-(\eta-1)^2 Z^2} \tag{7}$$

$$S_{21} = \frac{4\eta Z}{(\eta+1)^2-(\eta-1)^2 Z^2} \tag{8}$$

where the transmission term

$$Z = \exp(-jkd) \tag{9}$$

Consequently, if the slab is matched to free space with $\eta = \eta_0$, then $S_{11} = 0$ and $S_{21} = Z$. The identification of frequency regions where matching occurs is thus suggested when $|S_{11}| = 0$ and $|S_{21}| = 1$.

### 2.1 Double negative medium case 1

The MTM design process began with the desire to achieve CLS and SRR structures that would produce responses in the desired X-band region. Appropriately modified forms of the formulas given in [21] for the Jerusalem cross behavior were first used to obtain an estimate where the resonances of these structures would occur. These estimates dealt with the stripline widths, the gaps, the segment lengths and the periodicity of the elements. Because of the complex nature of the complete MTM with both the CLS and SRR structures present, it was expected that these initial estimates would only provide a rough approximation to the actual MTM behavior. An additional factor in the actual choice of the line widths and gaps was the suggestion that the best that I could do with some consistency as a novice with the required clean room etching process was approximately 5-10 mils ($1\,\text{mil} = 0.001\,\text{in} = 2.54 \times 10^{-3}\,\text{cm}$). In all the cases reported here, the line widths were 10 mils and the gaps were either 5 or 10 mils. Note that *mil*-units are quoted throughout as the standard because all of the fabrication processes were based on their use. Some useful conversion values are 100 mils $= .254$ cm and at 10 GHz, in free space $\lambda_0 = 3.0\text{cm} = 1,181$ mils and in a medium with $\varepsilon_r = 2.2$, $\lambda_m = \lambda_0/\sqrt{2.2} = 2.12\text{cm} = 835.2$ mils.

The dimensions of the CLS and SRR structures were finalized using the HFSS software tools. Each simulation model consisted of a two-port waveguide consisting of a pair of both perfect electric conductor (PEC) and perfect magnetic conductor (PMC) walls. A slab of dielectric material was centered in the waveguide. The input wave was launched in free space towards the slab at normal incidence from each port.

All inclusions were located on or in the slab; they were treated as infinitesimally thin and, hence, as PEC boundaries with $E_{tan} = 0$. This model allowed the effective simulation of a semi-infinite slab with an infinite periodic array of inclusions illuminated by a normally incident plane wave. All of the capacitor strips of the CLSs were perpendicular to the PEC walls; all of the SRR structures were parallel to the PMC walls. All S-parameter values were calculated.

The HFSS finalized dimensions of the CLS and SRR structures are indicated in Fig. 1. The CLSs were oriented with the main strip along the *y*-axis and the capacitor lengths along the *x*-axis. The SRRs lay in the *yz*-plane with the gap in the outer ring towards the source. The sizes associated with the CLSs were: every capacitor gap size was 10 mils and every line width was 10 mils; every CLS capacitor length was 130 mils, every CLS length was 140 mils, and the CLS period along the *y*-axis was 210 mils and along the *z*-axis was 150 mils. The sizes associated with the SRRs were: the outer square SRR side length was 100 mils, the inner square SRR side length was 70 mils, the distance between the inner and outer SRRs was 5 mils, and the SRR period between neighboring SRR centers in the *y*-direction was 110 mils and in the *z*-direction was 140 mils. The slab was filled with a $\varepsilon_r = 2.2$ dielectric substrate. The complete non-planar structure consisted of 5 CLSs and 4 SRRs in the unit cell. The first (last) CLS lay on the front (rear) face of the dielectric slab. Thus the total *z*-length of the slab (in the direction of propagation) was 560 mils. With a $\lambda$-refinement based upon a target frequency of 20 GHz, discrete sweeps were run between 5 and 15 GHz. The number of tetrahedra used was 54807 and gave a variation in the *S*-parameters of $\Delta S = 0.00458$.

The HFSS predicted magnitudes of $S_{11}$ and $S_{21}$ de-embedded to the front face of the dielectric region for the full MTM structure are shown in Fig. 2. Those for the same mesh with only the CLS inclusions (the SRRs were "turned off", i.e., the PEC boundary condition was not applied to them; hence, they were present in the geometry but they had no impact on the electromagnetic response of the structure) and only the SRR inclusions (the CLSs were "turned off") are given in Figs. 3a and 3b, respectively. From Fig. 3a one can see strong reflectivity turning on near 8 GHz and lasting until near 14 GHz. Similarly, from Fig. 3b one can see strong reflectivity turning on near 9 GHz and lasting until near 10 Ghz. The magnetic reflector behavior appears over a much narrower frequency range than does the electric response. Note that the phase of $S_{11}$ goes through zero at 9.635 GHz, hence, this SRR slab is responding like a PMC at that frequency. As shown in Fig. 2a and more closely in Fig. 2b, the composite MTM shows that there is matching over at least two narrow frequency bands near 9.8 GHz and 10.1 GHz. It is to be noted that when the CLS and SRR inclusions are combined together, they influence each other. If they were completely independent, one might have expected transmission in the entire band from 9-10 GHz where both the CLS and SRR responses show total reflectivity. Thus, both the CLS and SRR structures together impact the effective permittivity and permeability of the complete MTM. Note that simulations have shown that one

could achieve basically the same SRR behaviour with a single split ring. Thinner line widths and longer lines produce higher inductances, while smaller gaps produce more capacitance. The size of a single split ring can thus be adjusted to produce a similar resonant frequency behavior. The presence of the second split ring in the current configuration acts as another capacitive loading to the outer loop and thus helps to reduce the resonant frequency without impacting the overall size of the inclusion. Similarly, the resonant frequencies of the CLSs are lowered with thinner strips to produce higher inductances and with larger capacitor lengths to produce more capacitance.

The CLS-only and the SRR-only versions of the non-planar MTM were fabricated. Because of the costs and fabrication issues involved with the original 125 mil Rogers Duroid substrate design, all of the inclusions were etched on sheets of the 31 mil 5880 Rogers Duroid. Spacers consisting of $\varepsilon_r = 2.25$, 125 mil thick polyethylene were used to fill the voids to come as close as possible to the specified design distances. Thus one layer of the CLS structure was actually 31+125=156 mils rather than the 140 mil design; one layer of the SRR structure was actually 31+2(125) = 281 mils rather than the 210 mil design. A jig was available to house a 5.1 in. x 5.1 in. block of the MTM. This block was constructed by etching the Duroid, cutting all the polyethylene and Duroid pieces as close to the specifications as possible, drilling prescribed alignment holes, stacking all the layers along a polyethene rod inserted through their alignment holes and then milling the combined results to form a smooth MTM block.

A free space measurement system was used to test the MTM block. It consisted of two X-band 8.6 cm $\times$ 6.4 cm rectangular horns, one in transmit to illuminate directly at normal incidence the MTM block in the jig and one in receive. Free space measurements without the material under test (MUT) in place were taken to establish a reference. All of the *S*-parameters measurements were measured with a Hewlett-Packard 8720C network analyzer. The MTM MUT was then inserted into the jig. The measured values of $S_{21}$ for both the CLS-only and the SRR-only MTMs with the reference values backed out of the data are shown in Fig. 4. Despite the construction anomalies, there is a close correspondence between the measured $S_{21}$ values in Fig. 4 and the predicted values given in Fig. 3. There is a broad frequency region of high reflectivity in the CLS case; there is a narrow frequency band of high refelctivity in the SRR case. The upshifts in the values of these frequency regions were expected. The additional distances between the inclusions introduced by the spacers reduced their composite capacitances and inductances, causing the resonant frequencies to increase. The frequency regions where high reflectivity occurs in the CLS-only and the SRR-only MTMs are to be interpreted as those for which, respectively, the relative permittivity or permeability are negative.

### 2.2 Double negative medium case 2

Unfortunately, despite several conceptual attempts, it was decided that the complete non-planar MTM geometry could not be constructed given our laboratory's resources. Thus, another design was sought that was planar in nature, but had essentially the same inclusion shapes. The geometry of the resulting MTM unit cell is shown in Fig. 5. In this case, all gaps and all line widths were 10 mils. The unit cell in the *y*-direction was 160 mils; the height of the CLS inclusions was 150 mils. The length of the full capacitive strips was 140 mils; the length of the half strips was 70 mils. The length of the outer SRR was 110 mils; the length of the inner SRR was 70 mils. The unit cell in the *x*-direction was 125 mils. There was a 10 mil distance from the front and back face of the dielectric, $\varepsilon_r = 2.2$, to the first and last, respectively, CLSs. The *z*-length of the dielectric substrate was 590 mils.

This structure was again simulated with the normal incidence unit cell PEC-PMC waveguide configuration in HFSS. With a $\lambda$-refinement again based upon a target frequency of 20 GHz, discrete sweeps were run between 5 and 15 GHz. The number of tetrahedra used was 19586 and gave a variation in the *S*-parameters of $\Delta S = 0.00576$. Because this structure is planar and more symmetric itself, fewer tetrahedra were required in this simulation series. The HFSS predicted magnitudes of $S_{11}$ and $S_{21}$ de-embedded to the front face of the dielectric region are plotted in Fig. 6. There is clearly a regime where matching occurs which is zoomed in on in Fig. 7a. The corresponding phases are plotted in Fig. 7b. Matching occurs at 9.306 GHz, 10.142 GHz, and approximately at 10.904 GHz. The phases go to zero where the $S_{21}$ magnitude approaches one for the first two peaks.

This structure was also simulated with the commercial FDTD package produced by Ocotillo Electro-Magnetics [30]; it is based on the FDTD solver described in [31]-[33]. The code was modified to adapt the 2TDLM absorbing boundary conditions to mimic the unit cell PEC-PMC waveguide geometry used in the HFSS simulations. Cubical cells with side length $\Delta = 5$ mils were used in the FDTD simulations. A normally incident plane wave was launched from a total field/scattered field plane; the scattered electric fields were measured in front and behind the MTM slab. The total simulation space was 24 cells $\times$ 32 cells $\times$ 158 cells; the simulation was run for 20,000 time steps at a Courant value of 1.0. Some 80,000 time step runs at a Courant value of 0.5 were also made to double check the predicted behaviors. All of the smaller number of time step runs proved to be completely consistent with the larger total time step simulation results. The inclusions were treated as PECs on the faces of the cells. Thus, to achieve the desired symmetry in which the inclusions are centered in the simulation space, the distance in the *x*-direction was only 120 mils. Thus, some small differences between the HFSS and the FDTD results were anticipated. Nonetheless, the FDTD approach provides some complementary time domain information that was desired in understanding the physics of the MTM behavior.

The $S_{11}$ and $S_{21}$ values were obtained with the unit-cell FDTD simulator and de-embedded to the front face of the dielectric region. The magnitudes of these $S_{11}$ and $S_{21}$ values are plotted along with the HFSS values in Figs. 8a and 8b. Very good correlations between these simulation approaches applied to the MTMs are thus confirmed. One finds that the FDTD results are obtained much faster, but the dynamic frequency resolution provided by HFSS is better. The FDTD results could be made to produce a similar dynamic resolution but with a substantial increase in run time costs. Moreover, the FDTD results can be augmented with more complex substrate or inclusion behaviors, e.g., placing diodes across the capacitor gaps of all of the CLSs. Nonetheless, these results demonstrate the efficacy of both the HFSS and FDTD tools for MTM design.

The corresponding CLS-only and SRR-only MTM results for the magnitudes of $S_{11}$ and $S_{21}$ are provided in Figs. 9a and 9b. Again one finds that the CLS-only MTM produces high reflectivity above 8 GHz; the SRR-only MTM produces high reflectivity in the frequency range 8.4-10.2 GHz. The SRR-only MTM responds as a PMC ($S_{11} = +1$) at 9.238 GHz. There is better correlation between the frequency ranges of high reflectivity in these results and the complete planar MTM values. Nonetheless, there is again an upshift in the frequencies when all the inclusions are included, indicating some lowering of the overall inductance or capacitance values.

Experimentally, the complete planar and the SRR-only MTMs were constructed in the same manner as with the non-planar case. All the inclusions were etched on the 31 mil Rogers 5880 Duroid sheets; the MTM block was constructed with the aligned and etched Duroid sheets combined with polyethylene spacers; and it was tested at normal incidence with the free space measurement system described above. The reference corrected, experimentally-obtained $S_{21}$ values for these two MTM cases are shown in Fig. 10. Matching occurs with the complete MTM between 10.64 and 10.72 GHz. High reflectivity occurs with the SRR-only MTM in the region 9-11 GHz. Again, the experimental results are in favorable agreement with the simulations despite the differences between the simulated and the fabricated MTMs.

Thus, MTMs have been designed, fabricated, and tested and exhibit (at normal incidence) reflection and transmission properties that can be explained from the DNG media point of view, i.e., of having negative permittivity and permeability. However, these results themselves might be explained from other points of view. To provide a more definitive answer as to whether or not negative permittivities and permeabilities have been observed, the inverse problem of extracting effective material properties from the scattering data was considered.

## III. Effective medium parameters

To extract effective medium parameters from the normal incidence scattering parameter data, the Nicolson-Ross-Weir (NRW) approach, as described for instance in [34]-[38], was implemented. While many of the difficulties discussed in the literature are associated with sample sizes and the need for care when they are near a multiple of a half-wavelength, other problems were encountered when trying to apply these techniques to the MTMs under consideration here. Recall the definitions of $S_{11}$ and $S_{21}$ given, respectively, by Eqs. (7) and (8). The NRW approach begins by introducing the composite terms,

$$\begin{aligned} V_1 &= S_{21} + S_{11} \\ V_2 &= S_{21} - S_{11} \end{aligned} \tag{10}$$

and deriving the following quantities

$$X = \frac{1 + V_1 V_2}{V_1 + V_2} = \frac{1 + Z^2}{2Z} \tag{11}$$

$$Y = \frac{1 - V_1 V_2}{V_1 - V_2} = \frac{1 + \Gamma^2}{2\Gamma} \tag{12}$$

Consequently, one obtains from Eqs. (11) and (12)

$$Z = X \pm \sqrt{X^2 - 1} \tag{13}$$

$$\Gamma = Y \pm \sqrt{Y^2 - 1} \tag{14}$$

The choice of the sign is selected to maintain the expected magnitudes of these terms, i.e., $|Z| \leq 1$ and $|\Gamma| \leq 1$. In the MTM cases under consideration, the values of $S_{11}$ and $S_{21}$ are highly frequency dependent and achieve values near zero and unity. After testing them on numerous MTM cases, the standard extraction expressions were found to be unsatisfactory, particularly in the frequency regions where the permittivity and permeability resonances were expected, i.e., where those values would transition quickly between positive and negative values. The presence of the square root values is particularly difficult in those regions. One can not anticipate what branches the square root values should lie on without potentially biasing the end results.

Using the same process, however, one can derive many other expressions for $\Gamma$ and $Z$. Ones that could handle the current MTM cases were sought. For instance, one can obtain the transmission term $Z$ as:

$$Z = \frac{V_1 - \Gamma}{1 - \Gamma V_1} \tag{15}$$

Similarly, one can obtain the interface reflection coefficient as:

$$\Gamma = \frac{Z - V_2}{1 - ZV_2} \tag{16}$$

From Eqs. (16) and (15) one can obtain the exact expressions

$$1 - Z = \frac{(1 - V_1)(1 + \Gamma)}{1 - \Gamma V_1} \tag{17}$$

$$\eta = \frac{1 + \Gamma}{1 - \Gamma} = \frac{1 + Z}{1 - Z}\frac{1 - V_2}{1 + V_2} \tag{18}$$

Assuming that the electrical thickness of the MTM slab is not too large, i.e., that $k_{real}d \leq 1$, and knowing that the complex wavenumber $k = \omega\sqrt{\varepsilon_r\mu_r}/c = k_0\sqrt{\varepsilon_r\mu_r}$, one can write $Z \sim 1 - jkd$ to obtain the approximate results for the wave impedance and permeability from Eqs. (17) and (18), respectively,

$$k \sim \frac{1}{jd}\frac{(1 - V_1)(1 + \Gamma)}{1 - \Gamma V_1} \tag{19}$$

$$\mu_r \sim \frac{2}{jk_0d}\frac{1 - V_2}{1 + V_2} \tag{20}$$

The permittivity and index of refraction can then be obtained simply as

$$\varepsilon_r = \left(\frac{k}{k_0}\right)^2 \frac{1}{\mu_r} \tag{21}$$

$$n = \sqrt{\varepsilon_r\,\mu_r} = \frac{k}{k_0} \tag{22}$$

The square of the wave impedance can also be obtained as

$$\eta^2 = \frac{\mu_r}{\varepsilon_r} = \frac{Y + 1}{Y - 1} = \frac{1 + V_1}{1 - V_1}\frac{1 - V_2}{1 + V_2} = \frac{(S_{11} + 1)^2 - S_{21}^2}{(S_{11} - 1)^2 - S_{21}^2} \tag{23}$$

Because they avoid the square root issues, these expressions seemed to produce reasonable results for all the cases tested. Notice, however, that the combination of Eqs. (23) and (20) yields

$$\varepsilon_r \sim \frac{2}{jk_0d}\frac{1 - V_1}{1 + V_1}$$

This expression fails to reproduce the physically expected resonance features even though Eq. (20) does. It was found that some of the essential features exhibited by several formulas with $1 \mp V_1$ in them shared this issue when $S_{11} \to 0, 1$ while $S_{21} \to 1, 0$. These $V_1$ terms average the sharp features associated with $S_{11}$ and $S_{21}$.

It was found that even Eq. (21) is not as accurate as desired in all cases near the resonances of $\mu$ predicted by Eq. (20). The resonance features of $\varepsilon_r$ still become smeared. To overcome this difficulty, it was found that when $k_{real} d \leq 1$

$$S_{11} \quad \sim \quad \frac{2jkd\,(\eta^2 - 1)}{(\eta+1)^2 - (\eta-1)^2} = 2jkd\,\frac{\eta^2 - 1}{4\eta} \tag{24}$$

which yields

$$\varepsilon_r \quad \approx \quad \mu_r + j\,\frac{2S_{11}}{k_0 d} \tag{25}$$

This expression shows explicitly that $\varepsilon_r$ and $\mu_r$ should exhibit very similar responses when $S_{11} \to 0$.

The extraction formulas were applied to the various MTM cases to see if the resonant permittivity and permeability behaviors could be identified. Particular consideration was given to the extraction in those frequency regions where DNG behavior may have occurred. The assumption that $k_{real} d \leq 1$ with the extracted values was tested and was found to be satisfied in all of the cases reported below. Note that the resulting effective permittivities and permeabilities are to be interpreted in terms of how the MTM slab acts in reflection and transmission under normal incident plane wave illumination. Also note that other extraction approaches could have been attempted. For instance, one could assume models of $\varepsilon_r$ and $\mu_r$ and curve fit their coefficients to match the $S_{11}$ and $S_{21}$ behaviors. Despite the challenges associated with the NWR approach for these MTM cases, I felt that it was highly desirable to continue to deal with this established approach in order to connect the following results with known behaviors. Moreover, other approaches, e.g., the curve-fitting method, require an assumed medium model and could have led to unwanted biased final conclusions.

### 3.1 Double negative medium case 3

In order to test the extraction formulas, a simplified MTM test problem was designed. The resulting geometry is shown in Fig. 11. The unit cell consisted of one SRR sandwiched between two pairs of CLSs. Ideally, it was desired to have only one SRR and one pair of CLSs. However, when these inclusions were positioned in the same plane, large couplings between them occurred that were not present when they were simulated alone. Their separation into the split configuration shown in Fig. 11 produced the simplest *S*-parameter responses. Other MTM cases such as two pairs of SRRs and only one CLS produced more complex behavior

(e.g., two peaks instead of one). Note that with the symmetry walls, the actual configuration has two pairs of CLSs sandwiched between two SRRs. The dimensions of the inclusions were the same as in Sec. 2.2. The *y*-dimensions were all the same, the *y*-length of the slab being 160 mils. The *z*-length of the slab was thus only 290 mils. However, to further reduce the run times in the simulations and to remove potential issues for future fabrication efforts, the *x*-distance between any inclusion is 31 mils. Thus, the *x*-length of the slab was 93 mils. The smaller simulation space allowed for a finer $\Delta S$ value. The HFSS simulations of this MTM required 17,365 tetrahedra and produced a variation in the *S*-parameters of $\Delta S = 0.000626$ for the 20 GHz $\lambda$-refinement frequency.

The magnitudes of the HFSS-predicted values of $S_{11}$ and $S_{21}$ at normal incidence for this simplified cell MTM are shown in Figs. 12a and 12b. The response has been reduced to a single feature. The peak of this feature in $S_{21}$ occurs at 9.503 GHz, as shown in Fig. 12b. Applying Eqs. (20), (21), and (22) to these results, one obtains the real parts of the permeability and permittivity given in Fig. 13a, and the real and imaginary parts of the index of refraction given in Fig. 13b. As shown in Fig. 13a, the permittivity and permeability go through a resonance where $S_{21}$ peaks and have nontrivial negative values there. Moreover, as shown in Fig. 13b, the real part of the index of refraction is also negative there. The imaginary part of the index of refraction is also given to demonstrate that the extraction process yields physical values, i.e., the imaginary part is less than zero. With many other versions of the extraction formulas, this does not occur. From Fig. 13a it is readily apparent why the structure would be reflecting slightly away from the matching point since the permittivity has large negative values there. The form of the curve for the permittivity except near the matching point resembles a Drude response; this metal-like description correlates nicely with the large negative values of the permittivity and the corresponding large reflectivity. The matching region around the peak of the $|S_{21}|$ curve is shown in Fig. 14a. As anticipated above, one can see that the agreement between the permittivity and permeability values is marginal there. Again, this is believed to result from the differences between the extraction formulas for $\varepsilon_r$ and $\mu_r$ and their particular dependencies on $V_1$ and $V_2$ in that region. On the other hand, making use of Eq. (25), which is appropriate for $|S_{11}| \sim 0$, to re-calculate the permittivity, one obtains the comparison shown in Fig. 14b. These results demonstrate a nice matching between the behaviors of the permeability and permittivity where $|S_{21}| \sim 1$. Moreover, points on the high frequency side of where $|S_{21}|$ peaks correspond to where the permeability and permittivity and, hence, the index of refraction are most negative.

To understand the behavior of the corresponding CLS-only and SRR-only MTMs, the associated *S*-parameters were obtained from the corresponding HFSS simulations. The magnitudes of $S_{11}$ and $S_{21}$ for the CLS-only MTM are given in Fig. 15a; the extracted real part of the permittivity is shown in Fig. 15b. The Drude-like behavior mentioned above is very apparent. However, the expected Lorentz-like behavior

near the matching point of the complete MTM was not apparent. With a finer discrete frequency sweep in that region, the extraction process shows the presence of small resonance features at 8.903 and 9.02 GHz, corresponding to the barely discernible features in the $S_{21}$ curve in Fig. 15a. It is believed that the presence of the SRRs in the complete MTM enhances the response of these resonance features to achieve the matching shown in Fig. 14b. Note also that the mentioned small features in $S_{21}$ indicate that this CLS-only configuration has some non-trivial magnetic properties to it as well. This would be expected since one planar pair of CLSs forms a ring with two splits and should respond to the presence of the magnetic field.

The corresponding magnitudes of $S_{11}$ and $S_{21}$ for the SRR-only MTM are given in Fig. 16a; the extracted real part of the permeability is shown in Fig. 16b. The permeability has a strong resonance behavior around 8.46 GHz; it takes on negative values near 8.673 GHz where the reflectivity of this MTM peaks. The phases of $S_{11}$ and $S_{21}$ for the SRR-only MTM are given in Fig. 16c. One finds that the phase of $S_{11}$ goes to zero at the resonance point of the real part of the permeability. The magnitude of the reflection coefficient $|S_{11}| \sim 0.964$ there. Thus, the SRR-only MTM can be characterized as a magnetic conductor in this region.

Note that it was hoped that the permittivity and permeability results would clarify which type of resonances were present in the data: Lorentz or Drude or 2TDLM. Unfortunately, not all the features present could be fit with a single model. Moreover, with infinitesimally thin PEC inclusions in the simulations, the loss terms in those models could not be used to help settle the issue. The 2TDLM model appeared to be the best approximation to the SRR-only MTM permeability results shown in Fig. 16b; a 2TDLM model appeared to be the best approximation to the complete MTM permittivity and permeability results shown in Fig. 14b; and a Drude model (modulo the small superimposed Lorentz-like resonances) appeared to be the best approximation to the CLS-only MTM permittivity results shown in Fig. 15b. Geometries that would clarify these resonance model considerations are currently under investigation.

### 3.2 Double negative medium case 2

Consider again the planar DNG MTM. Applying Eqs. (20) and (25) to the *S*-parameter results, one obtains the curves shown in Fig. 17 for the real parts of the permeability and permittivity. One can see that there are three regions of interest corresponding to the three peaks in the $|S_{21}|$ values. Applying a pole-residue identification approach to the FDTD data for this MTM [39], one finds the presence of three strong poles where these peaks occur (using MATLAB 6.0, with the Signal Processing Toolbox and the System Identification Toolbox, the extraction followed an output-error model to identify the coefficients in a difference equation whose solutions yields the poles and residues, as shown in [40]). On the other hand, the permittivity and permeability data indicates the presence of two strong resonance lines corresponding to the first and third peaks of $|S_{21}|$. The first peak corresponds to a narrow resonance with a very strong matching of the permit-

tivity and permeability behaviors. The third peak shows a much broader resonance with a weaker matching behavior. The second peak occurs where there is matching, but the permittivity and permeability behaviors are basically small and flat in their frequency response.

To show that matching has occurred at least at the first two resonances, the magnitude of $\eta^2 = \mu_r/\varepsilon_r$ obtained from the HFSS-generated S-parameters and from Eq. (23) is presented in Fig. 18. The magnitude of $S_{21}$ is also provided for comparison. The impedance clearly goes through unity at the peaks of the transmission data showing matching occurs at least there.

The associated values of the real part of the index of refraction extracted directly from the HFSS *S*-parameter results are shown in Fig. 19a. The corresponding FDTD results are shown in Fig. 19b. These were obtained from the Fourier transform of electric fields generated in the 80,000 time step, 0.5 Courant value simulation at an observation point, $\vec{r}_{obs}$, beyond the planar MTM slab whose depth is $d_{slab}$ when the MUT is present and when it is not as:

$$n_{re} = \frac{1}{-jk_0 d_{slab}} \ln\left[\frac{E_{MTM}(\vec{r}_{obs},\omega)\, e^{-jk_0 d_{slab}}}{E_{free\ space}(\vec{r}_{obs},\omega)}\right] \tag{26}$$

The values of $n_{re}$ were also obtained independently by D. Dudley. [39] Again, using MATLAB 6.0, with the Signal Processing Toolbox and the System Identification Toolbox, he applied a frequency-domain Wiener filter [41] to obtain the transfer function of the slab. The spectral data being Wiener-filtered was obtained from Fourier transforms of the FDTD simulation results and was first decimated to 1020 points based on the Nyquist frequency, estimated from the natural filtering characteristic of the input signal. While they are not identical and all are noisy, there are important correspondences amongst these three results. In particular, note that the index is indeed negative after the first material resonance location, passing through zero and becoming positive at the second peak of $|S_{11}|$, until the second material resonance location is reached. This can occur only if both the permittivity and permeability are negative there. Before and beyond these resonances, the HFSS result is zero and the FDTD result oscillates about zero. Because of the strong correlation between the simulated and measured *S*-parameter results, the experimentally tested planar MTM, therefore, will also exhibit strong DNG properties in this region.

It is to be noted that the experimentally measured phase values were too noisy for a direct application of the extraction formulas to the experimental data. Even the phase data generated from the FDTD simulation results was too noisy. The extraction formula are very sensitive to any phase variations. Improved phase measurements and less sensitive extraction formulas are needed. Moreover, because these MTMs are anisotropic, they all need to be studied under oblique illumination to characterize their behavior completely. These issues continue to be under investigation.

## IV. Conclusions

It was demonstrated that DNG metamaterials can be designed, fabricated, and tested with normal microwave engineering tools. Both HFSS and FDTD calculations of DNG MTMs illustrated their properties. Metamaterials consisting of CLS and SRR inclusions were introduced. Slabs of non-planar and a planar types of MTMs with these CLS and SRR inclusions were fabricated. Both MTMs were tested with reasonable comparisons between the predicted and measured results. More costly and more accurate fabrication processes should lead to more precise comparisons.

A set of effective material parameter extraction formulas were derived from the reflection and transmission data for normally incident plane wave illumination and were applied to the MTM results from the HFSS simulations. A simpler MTM geometry was introduced for application of these extraction formulas. It was shown that both the permittivity and permeability exhibit strong resonance regions and become negative there. Metamaterials with mainly dielectric and magnetic properties were presented as special cases of the complete MTM. Magnetic conductor properties were demonstrated with the SRR-only MTM special case. Moreover, the complete, simple MTM example showed that matching can be achieved. Application of this material parameter extraction process to the more complex planar MTM demonstrated that it too achieves the DNG and matching properties. Thus, the corresponding fabricated planar MTM slab would also.

Other MTM designs are currently being studied. Their integration into a number of antenna and sensor applications are currently under investigation and will be discussed in future publications.

**Acknowledgments:** The author would like to thank Dr. Mike Hill, INTEL Corp., for his help with the first series of measurements, and Mr. Robert Hsu for his help with the second series of measurements. He would like to thank Dr. David C. Wittwer, President of Ocotillo ElectroMagnetics, Inc., for modifying OEM's FDTD simulator to handle the PEC-PMC waveguide unit cell configuration used in this MTM study. The author would also like to extend special thanks to Prof. Don Dudley for his time and efforts into the processing of the FDTD signals to determine independently the index of refraction of the planar MTM and for the results appearing in Fig. 19b. The author would also like to thank the reviewers for several valuable suggestions that led to improvements in this paper.

## References


[1] V. G. Veselago, “The electrodynamics of substances with simultaneously negative values of ε and $\mu$,” *Sov. Phys. Uspekhi*, vol. 10, no. 4, pp. 509-514, Jan-Feb. 1968.

[2] H. Kosaka, T. Kawashima, A. Tomita, M. Notomi, T. Tamamura, T. Sato, and S. Kawakami, “Super-prism phenomena in photonic crystals,” Phys. Rev. B, vol. 58, pp. R10096-10099, 15 October, 1998.

[3] J. B. Pendry, “Negative Refraction Makes a Perfect Lens,” *Phys. Rev. Lett.*, vol. 85, no. 18, pp. 3966-3969, 30 October 2000.

[4] J. B. Pendry, A. J. Holden, D. J. Robbins, and W. J. Stewart, “Magnetism from conductors and enhanced nonlinear phenomena,” IEEE Trans. Microwave Theory Tech., vol. 47, no. 11, pp. 2075-2084, November 1999.

[5] D. R. Smith and N. Kroll, “Negative refractive index in left-handed materials,” *Phys. Rev. Lett.*, vol. 85, no. 14, pp. 2933-2936, October 2000.

[6] R. A. Shelby, D. R. Smith, S. C. Nemat-Nasser, and S. Schultz, “Microwave transmission through a two-dimensional, isotropic, left-handed metamaterial,” *Appl. Phys. Lett.*, vol. 78, no. 4, pp. 489-491, January 2001.

[7] R. A. Shelby, D. R. Smith, and S. Schultz, “Experimental verification of a negative refractive index of refraction,” *Science*, vol. 292, pp. 77-79, April 2001.

[8] R. W. Ziolkowski, “Superluminal transmission of information through an electromagnetic metamaterial,” *Phys. Rev. E*, vol. 63, 046604 (2001).

[9] J. D. Joannopoulos, R. D. Meade, and J. N. Winn, *Photonic Crystals: Molding the Flow of Light*, (Princeton University Press, Princeton, NJ, 1995).

[10] R. W. Ziolkowski and E. Heyman, “ Wave propagation in media having negative permittivity and permeability,” Phys Rev. E, vol. 64, 056625, pp. 1-15, October 30, 2001.

[11] R. W. Ziolkowski, “The design of Maxwellian absorbers for numerical boundary conditions and for practical applications using engineered artificial materials,” *IEEE Trans. Antennas and Propagat.*, vol. 45(4), pp. 656-671, April 1997.

[12] R. W. Ziolkowski, “Time-derivative Lorentz materials and their utilization as electromagnetic absorbers,” *Phys. Rev. E*, vol. 55(6), pp. 7696-7703, June 1997.

[13] R. W. Ziolkowski, "Time-derivative Lorentz material model-based absorbing boundary condition," *IEEE Trans. Antennas and Propagat.*, vol. 45(10), pp. 1530-1535, October 1997.

[14] R. W. Ziolkowski, "Maxwellian Material Based Absorbing Boundary Conditions," *Comp. Meth. Appl. Mech. Eng.*, vol. 169, no. 3-4, pp. 237-62, February 1999.

[15] R. W. Ziolkowski and F. Auzanneau, "Passive artificial molecule realizations of dielectric materials," *J. Appl. Phys.*, vol. 82, no. 7, pp. 3195-3198, October 1997.

[16] R. W. Ziolkowski and F. Auzanneau, "Artificial molecule realization of a magnetic wall," *J. Appl. Phys.*, vol. 82, no. 7, pp. 3192-3194, October 1997.

[17] F. Auzanneau and R. W. Ziolkowski, "Étude théorique de matériaux bianisotropes synthétiques contrôlables," *J. Phys. III*, vol. 7, pp. 2405-2418, December 1997.

[18] F. Auzanneau and R. W. Ziolkowski, "Theoretical study of synthetic bianisotropic smart materials," *Journal of Electromagnetic Waves and Applications*, vol. 12, no. 3, pp. 353-370, March 1998.

[19] T. K. Wu, *Frequency Selective Surface and Grid Array*, John Wiley & Sons, Inc., New York, 1995.

[20] B. A. Munk, *Frequency Selective Surfaces*, John Wiley & Sons, Inc., New York, 2000.

[21] I. Anderson, "On the theory of self-resonant grids," B. S. J. T., vol. 54, no. 10, pp. 1725-1731, December 1975.

[22] R. E. Collin, "Field Theory of Guided Waves," 2nd Ed., (IEEE Press, Piscataway, NJ, 1990), Chap. 12, pp. 749-786.

[23] N. Marcuvitz, *Waveguide Handbook*, M. I. T. Radiation Laboratory Series, vol. 10, New York, 1951, pp. 284-286.

[24] S. B. Cohn, "The electric and magnetic constants of metallic delay media containing obstacles of arbitrary shape and thickness," J. Appl. Phys., vol. 22, no. 5, pp. 628-634, May 1951.

[25] J. Brown, "Artificial dielectrics having refractive indices less than unity," Proc. IEE (London), vol. 100, Part IV, pp. 51-62, May 1953.

[26] J. Brown and W. Jackson, "The properties of artificial dielectrics at centimetre wavelengths," Proc. IEE (London), vol. 102, Part B, pp. 11-16, January 1955.

[27] W. Rotman, “Plasma simulation by artificial dielectrics and parallel-plate media,” IRE Trans. Antennas Propagat., vol. 10, pp. 82-95, January 1962.

[28] S. W. Lee, G. Zarillo, and C.-L. Law, “Simple formulas for transmission through periodic metal grids or plates,” IEEE Trans. Antennas Propagat., vol. AP-30, no. 5, pp. 904-909, September 1982.

[29] C. A. Balanis, *Antenna Theory*, 2nd Ed., John Wiley & Sons, Inc., New York, 1982, pp. 214-217.

[30] Ocotillo ElectroMagnetics, Inc. 1889 W. Queen Creek Rd. Apt. #2109 Chandler, AZ 85248

[31] D. C. Wittwer and R. W. Ziolkowski, “Two time-derivative Lorentz material (2TDLM) formulation of a Maxwellian absorbing layer matched to a lossy media,” *IEEE Trans. Antennas and Propagat.*, vol. 48, no. 2, pp. 192-199, February 2000.

[32] D. C. Wittwer and R. W. Ziolkowski, “Maxwellian material based absorbing boundary conditions for lossy media in 3D,” *IEEE Trans. Antennas and Propagat.*, vol. 48, no. 2, pp. 200-213, February 2000.

[33] D. C. Wittwer and R. W. Ziolkowski, “The effect of dielectric loss in FDTD simulations of microstrip structures,” *IEEE Trans. Microwave Theory Tech.*, vol. 49, no. 2, pp. 250-262, February 2001.

[34] A. M. Nicolson and G. F. Ross, “Measurement of the intrinsic properties of materials by time domain techniques,” IEEE Trans. Instrumentation and Measurement, vol. IM-19, no.4, pp. 377-382, November 1970.

[35] W. B. Weir, “Automatic measurement of complex dielectric constant and permeability at microwave frequencies,” Proc. IEEE, vol. 62, pp. 33-36, January 1974.

[36] P. K. Kadaba, “Simultaneous measurement of complex permittivity and permeability in the millimeter region by a frequency-domain technique,” IEEE Trans. Instrumentation and Measurement, vol. IM-33, no.4, pp. 336-340, December 1984.

[37] D. K. Ghodgaonkar, V. V. Vradan, and V. K. Varadan, “Free-space measurement of complex permittivity and complex permeability of magnetic materials at microwave frequencies,” IEEE Trans. Instrumentation and Measurement, vol. 39, no.2, pp. 387-394, April 1990.

[38] J. Baker-Jarvis, E. J. Vanzura, and W. A. Kissick, “Improved techniques for determining complex permittivity with the transmission/reflection method,” IEEE. Trans. Microwave Theory Tech., vol. 38, no. 8, pp. 1096-1103, August 1990.

[39] Donald G. Dudley, private communications, Tucson, AZ.

[40] L. Ljung and T. Soderstrom, *Theory and Practice of Recursive Identication,* MIT Press, Boston, MA, 1983, pg. 52-54.

[41] A. K. Jain, *Fundamentals of Digital Image Processing,* Prentice-Hall, Englewood Cliffs, NJ, 1989, pg. 275-284.

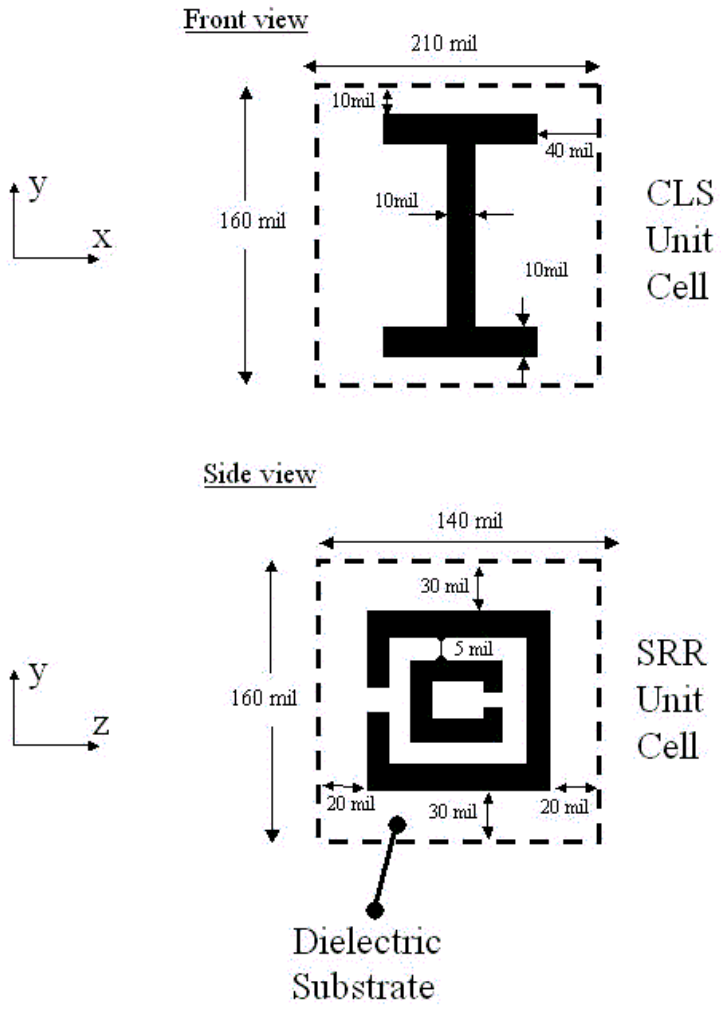


Figure 1: Non-planar MTM geometry.

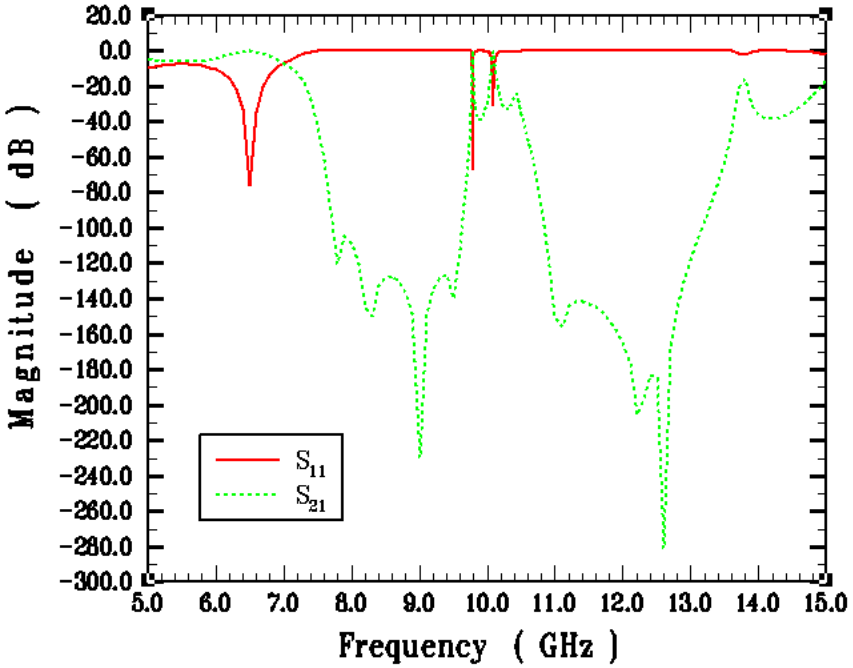


Fig. 2a. Magnitudes of $S_{11}$ and $S_{21}$

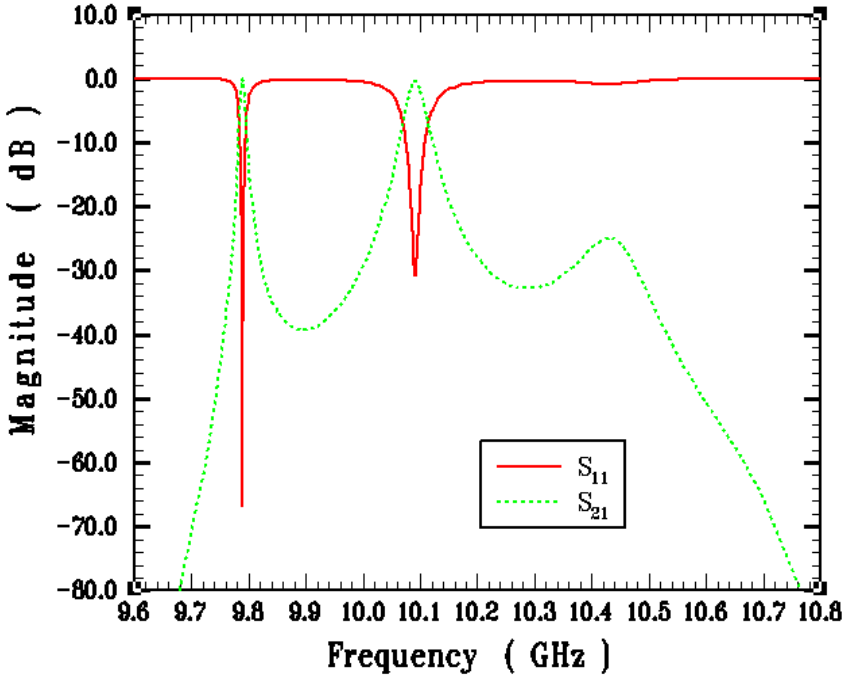


Fig. 2b. Zoom

Figure 2: HFSS-predicted S-parameters for the non-planar MTM.

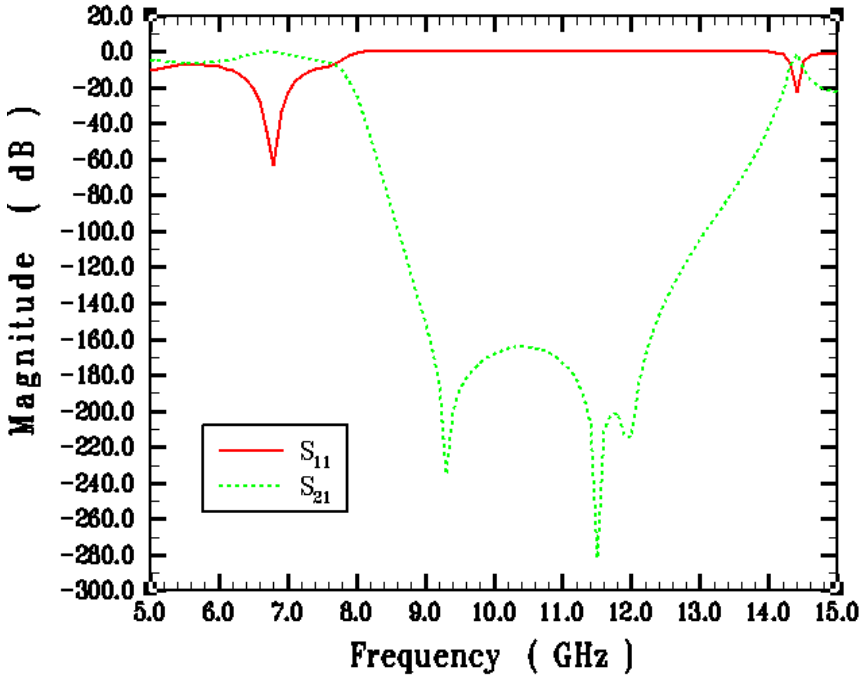


Fig. 3a. CLS-only MTM

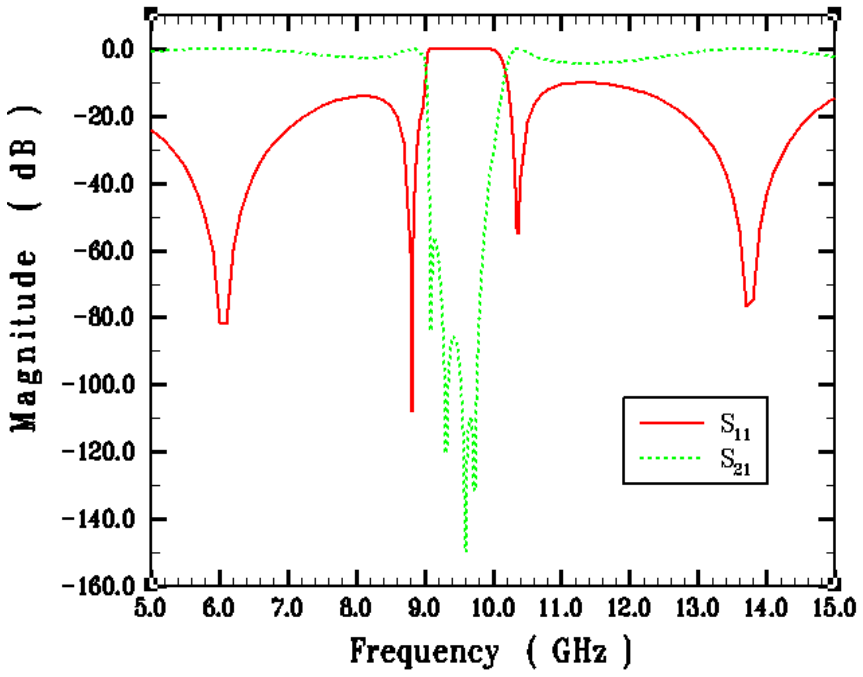


Fig. 3b. SRR-only MTM

Figure 3: Magnitudes of the HFSS-predicted S-parameters for the restricted MTM cases corresponding to Fig. 2.

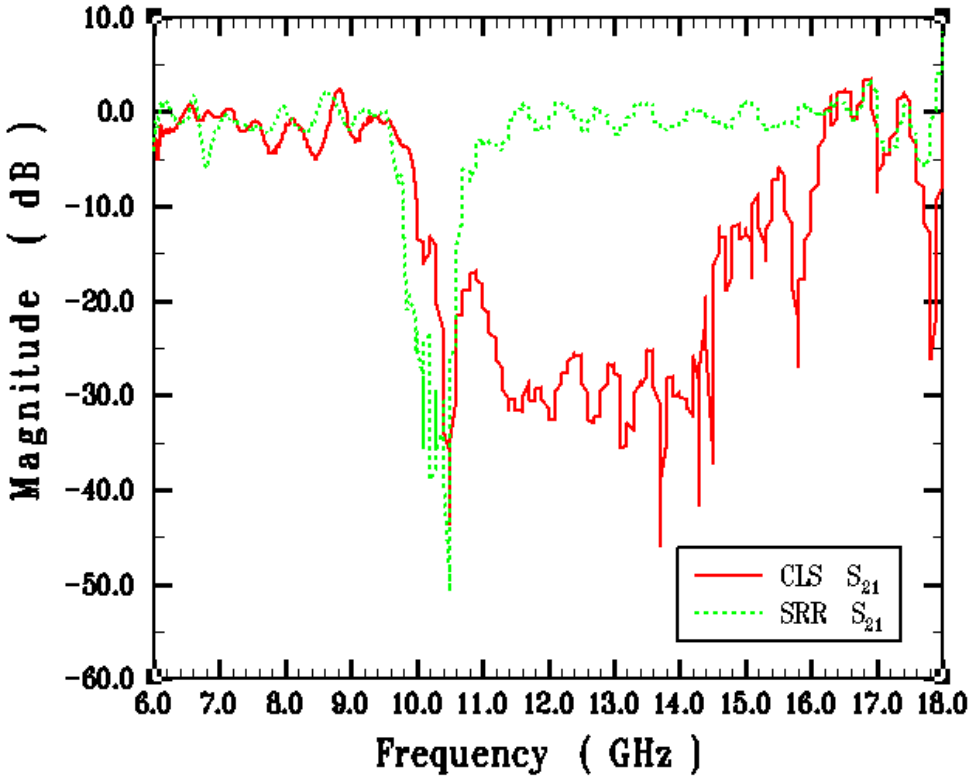


Figure 4: Magnitudes of the experimentally measured $S_{21}$ values for the CLS-only and SRR-only MTM cases shown in Figs. 3a and 3b.

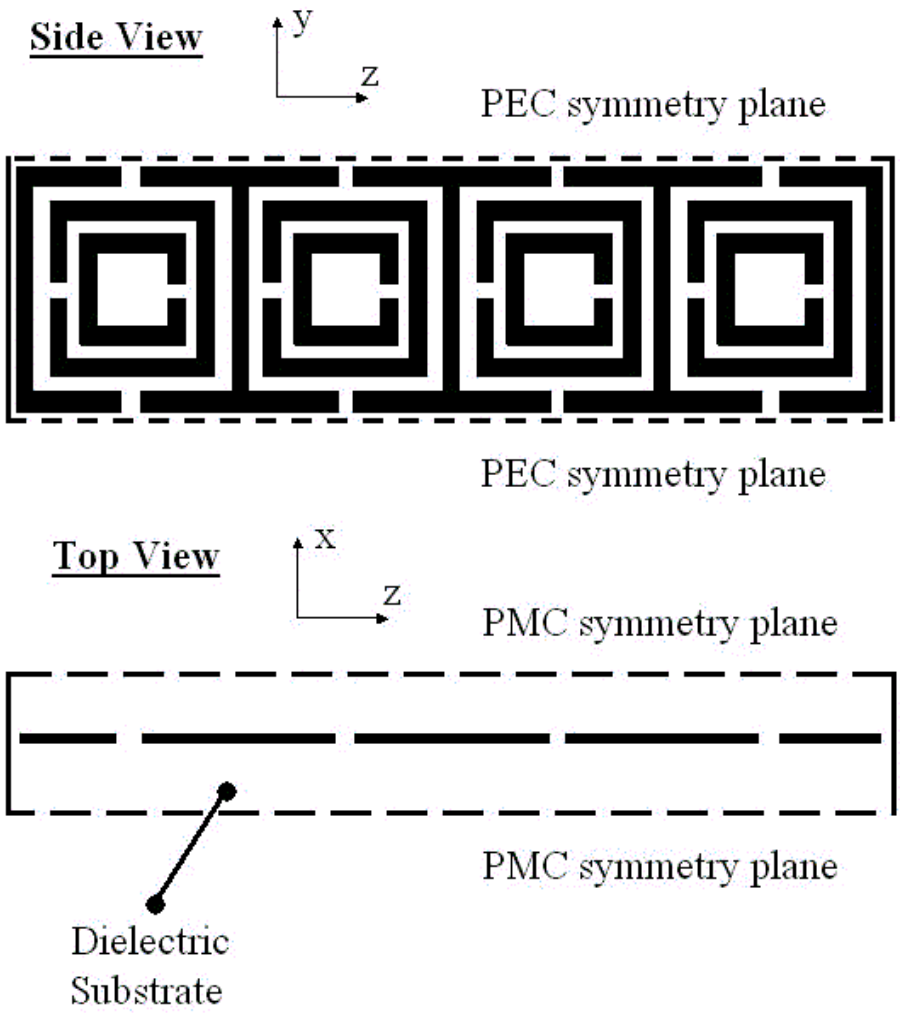


Figure 5: Planar MTM geometry.

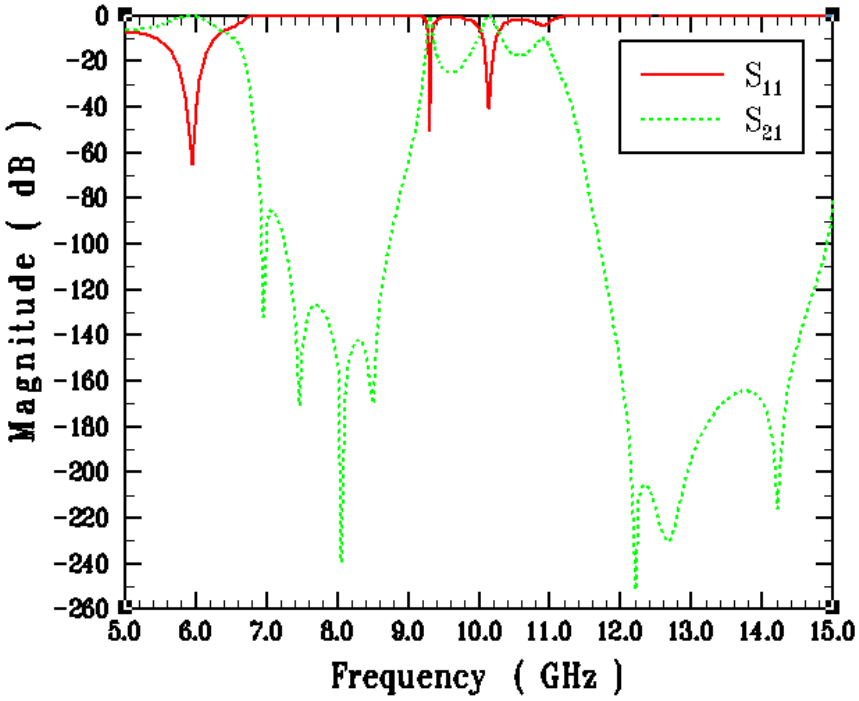


Figure 6: Magnitudes of the HFSS-predicted S-parameters for the complete planar MTM.

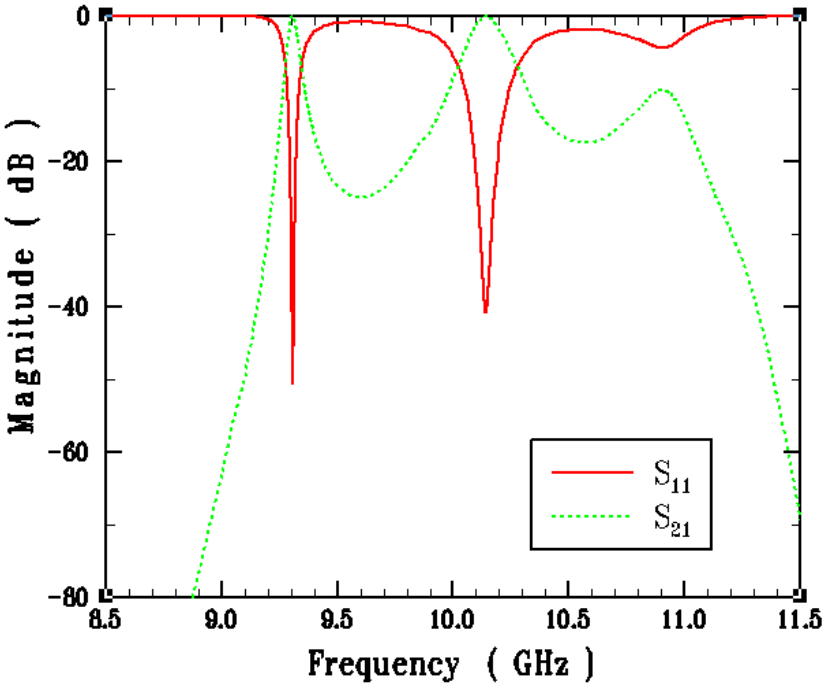


Fig. 7a. Zoom of the magnitudes

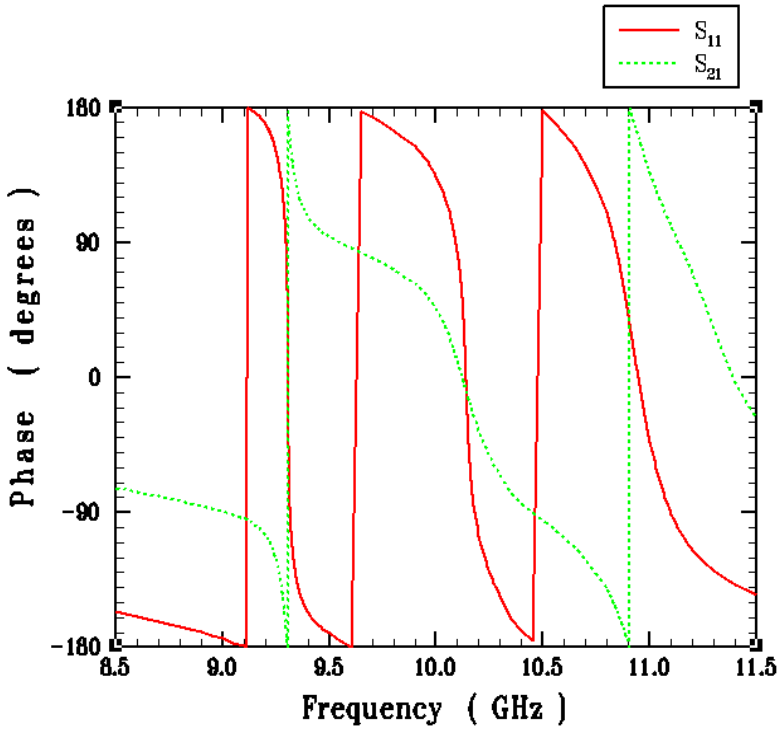


Fig. 7b. Zoom of the phases

Figure 7: HFSS-predicted S-parameters for the complete planar MTM shown in Fig. 6a.

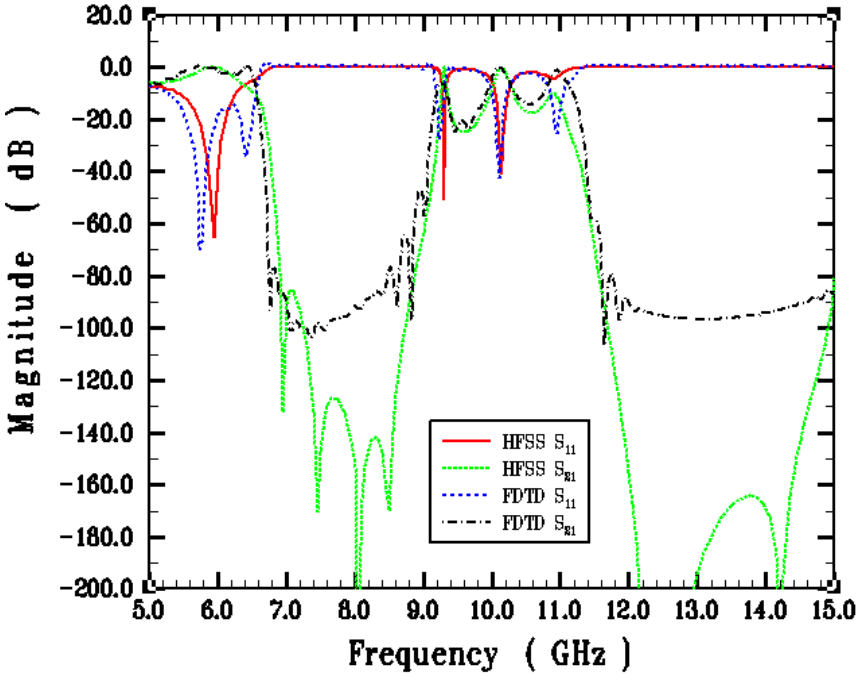


Fig. 8a. Magnitudes

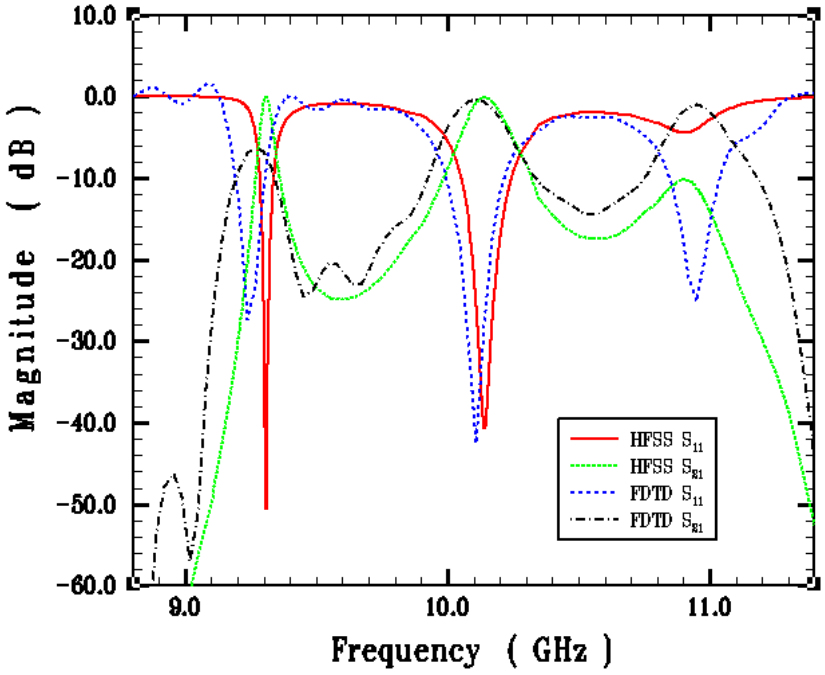


Fig. 8b. Zoom

Figure 8: Comparison of the HFSS- and FDTD-predicted S-parameters for the complete planar MTM.

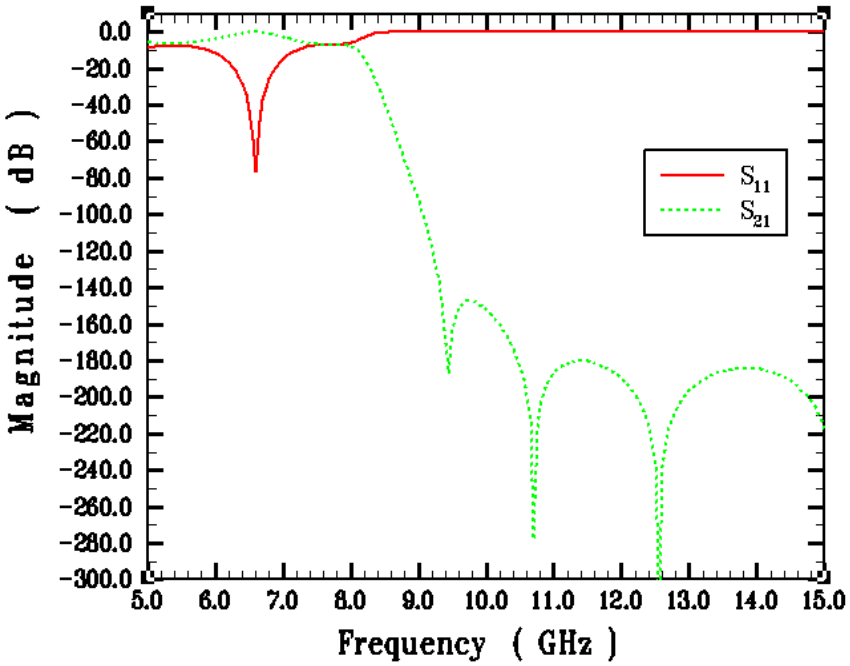


Fig. 9a. CLS-only

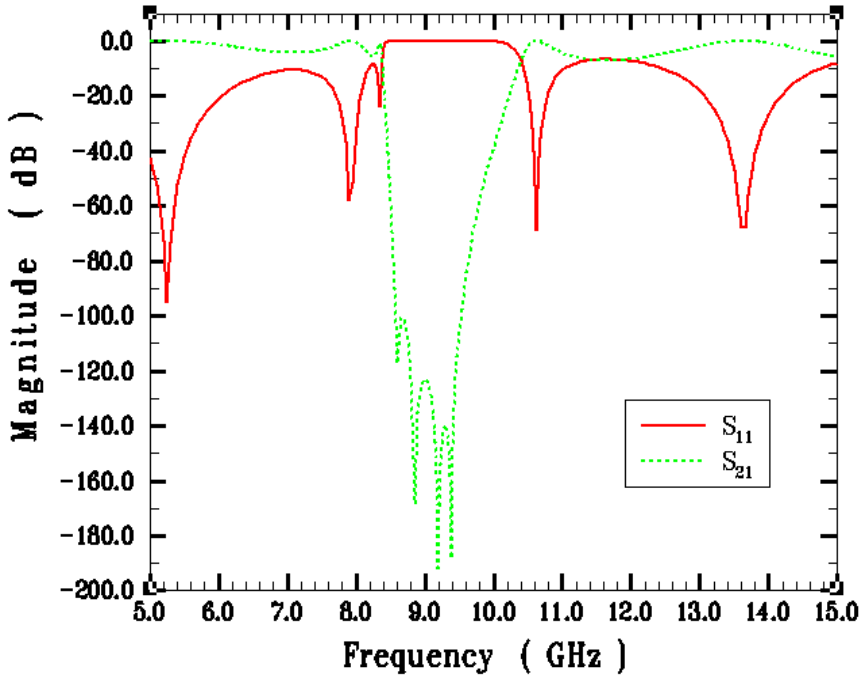


Fig. 9b. SRR-only

Figure 9: Magnitudes of the HFSS-predicted S-parameters for the restricted planar MTM cases

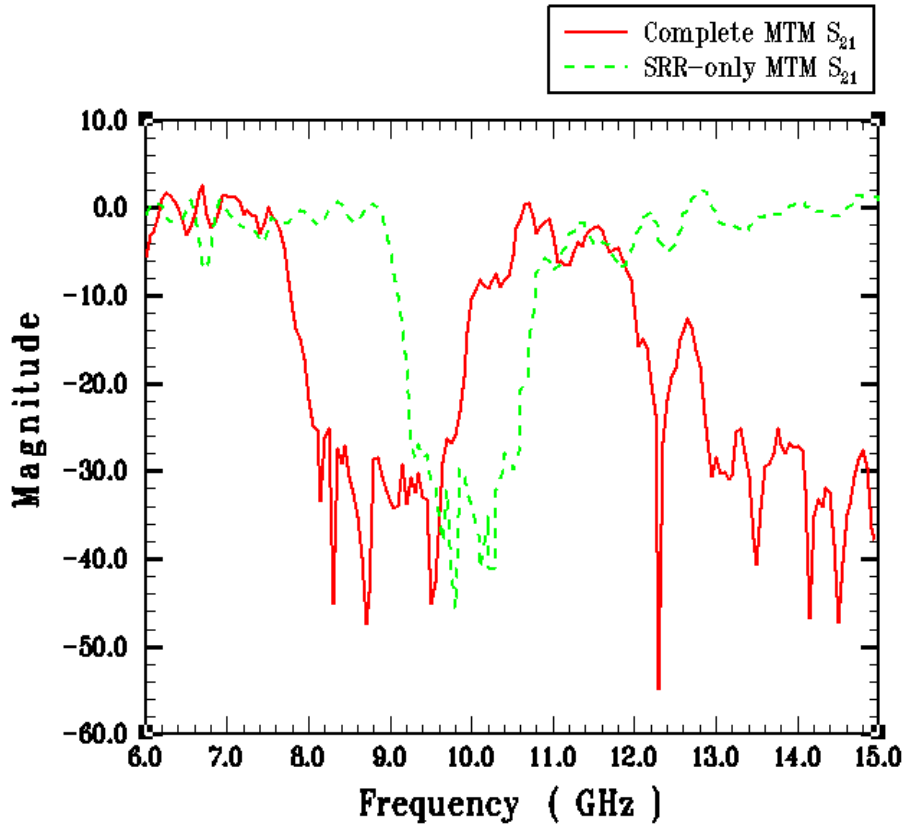


Figure 10: Magnitude of the experimentally measured $S_{21}$ values for the complete planar MTM and for the corresponding SRR-only MTM.

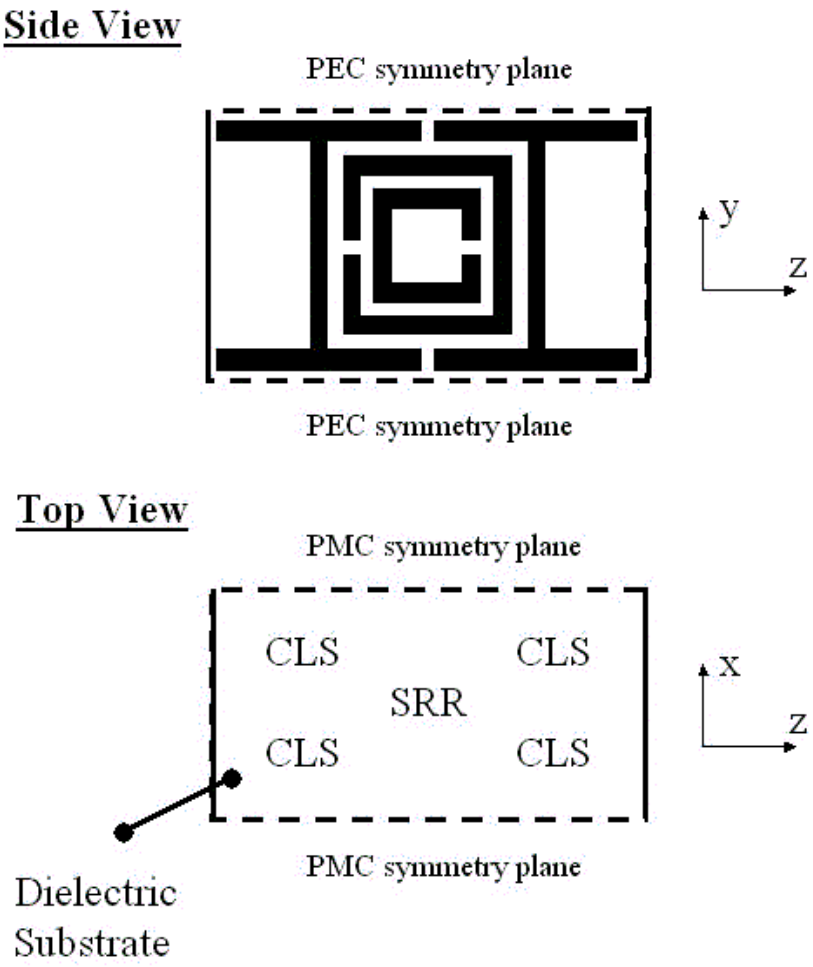


Figure 11: Simplified non-planar MTM geometry used to test the material extraction procedure.

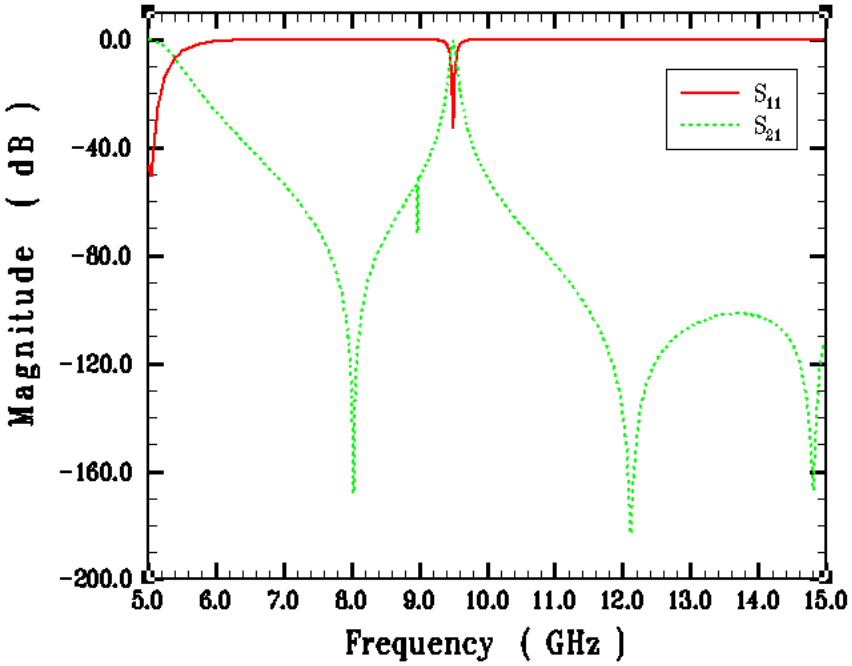


Fig. 12a. Magnitudes

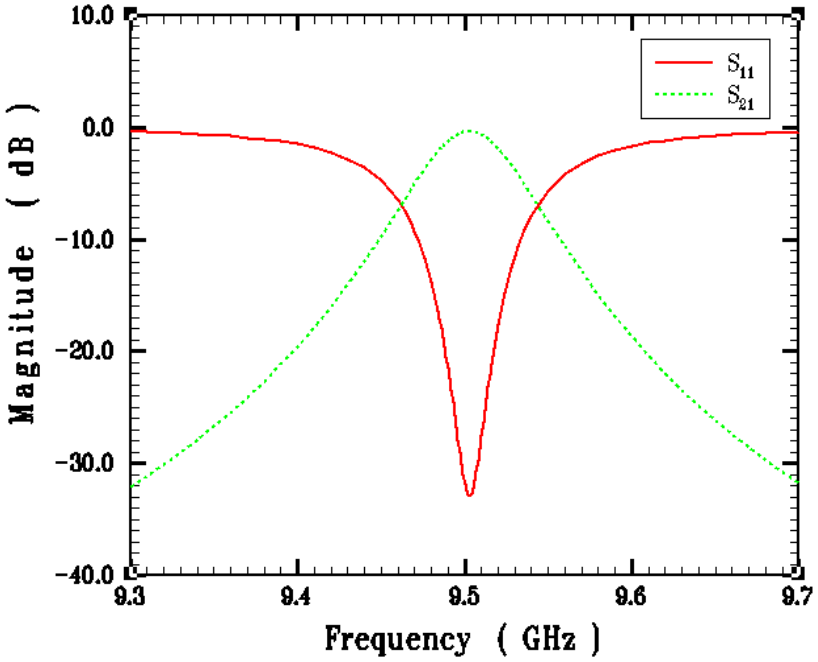


Fig. 12b. Zoom

Figure 12: HFSS-predicted S-parameters for the complete MTM with the simplified unit cell.

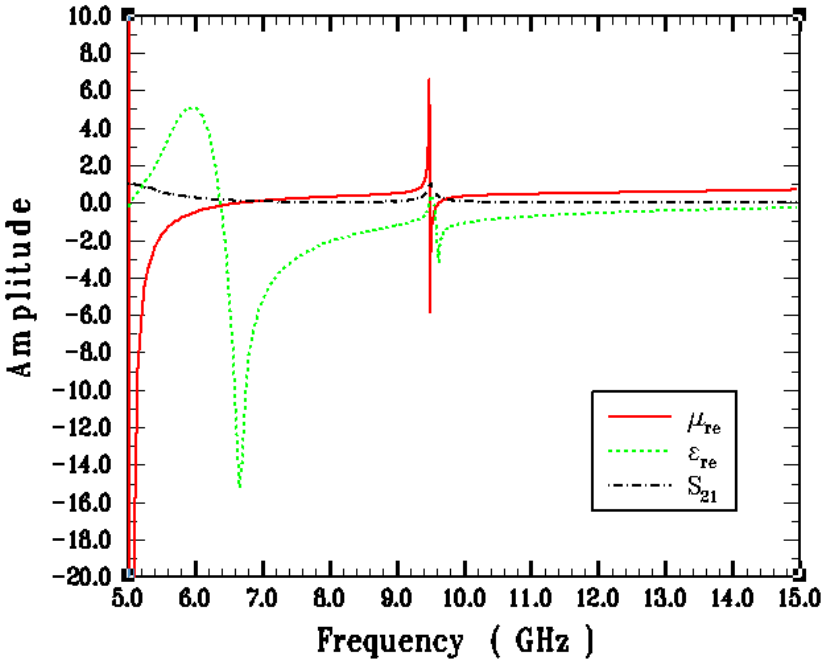


Fig. 13a. Real parts of the permittivity and permeability

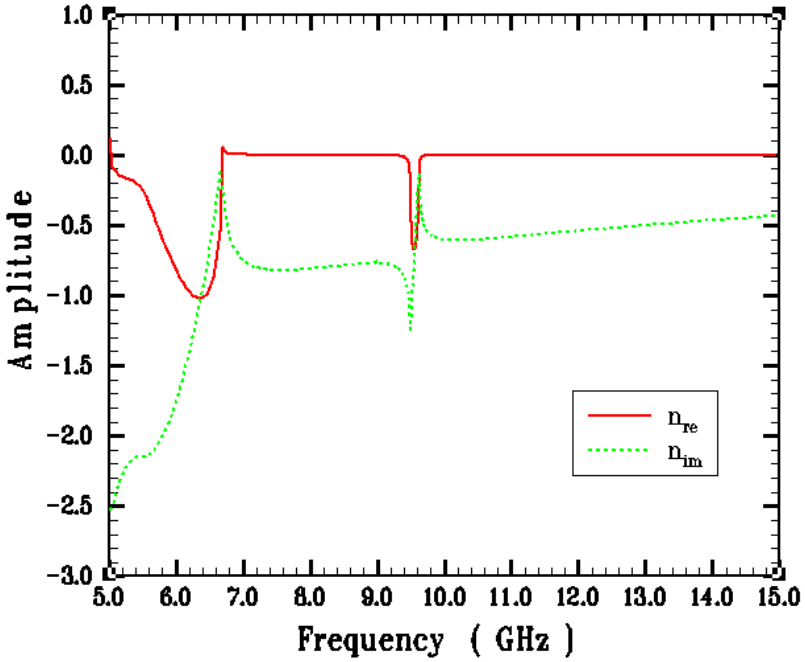


Fig. 13b. Index of refraction

Figure 13: Extracted parameters for the complete MTM with the simplified unit cell.

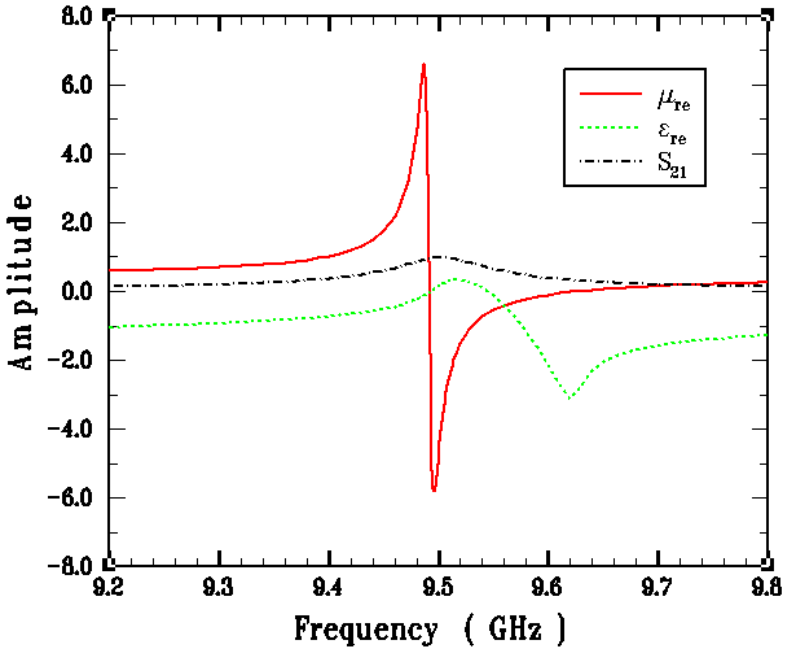


Fig. 14a. Zoom of the amplitudes shown in Fig. 13a

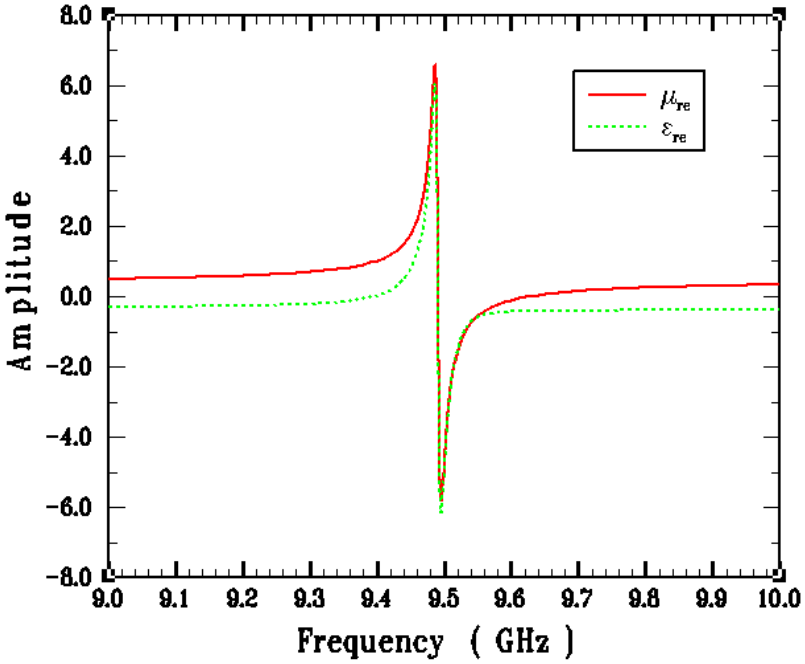


Fig. 14b. Corrected local predicted permittivity and permeability values

Figure 14: More extracted parameters for the complete MTM with the simplified unit cell.

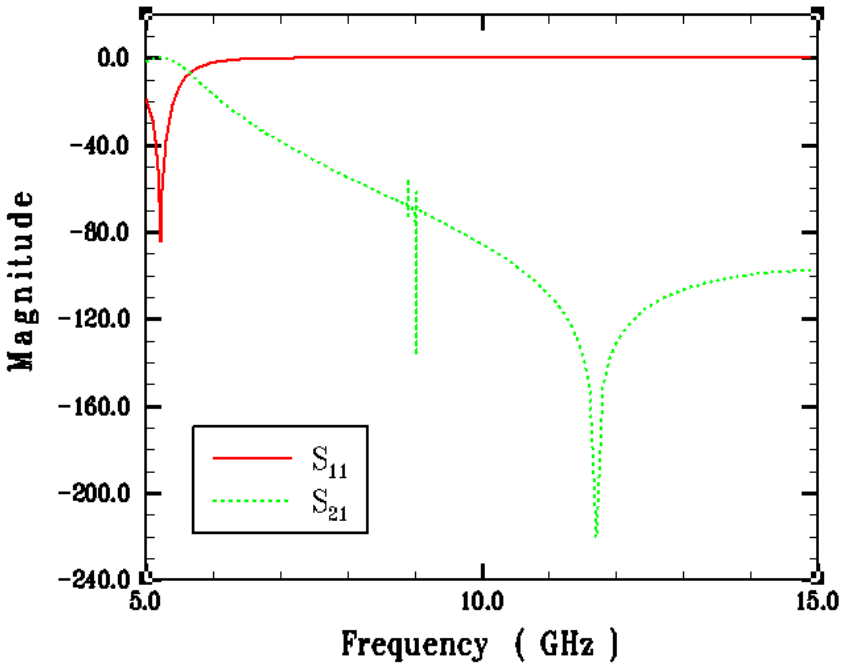


Fig. 15a. Magnitudes of the S-parameters

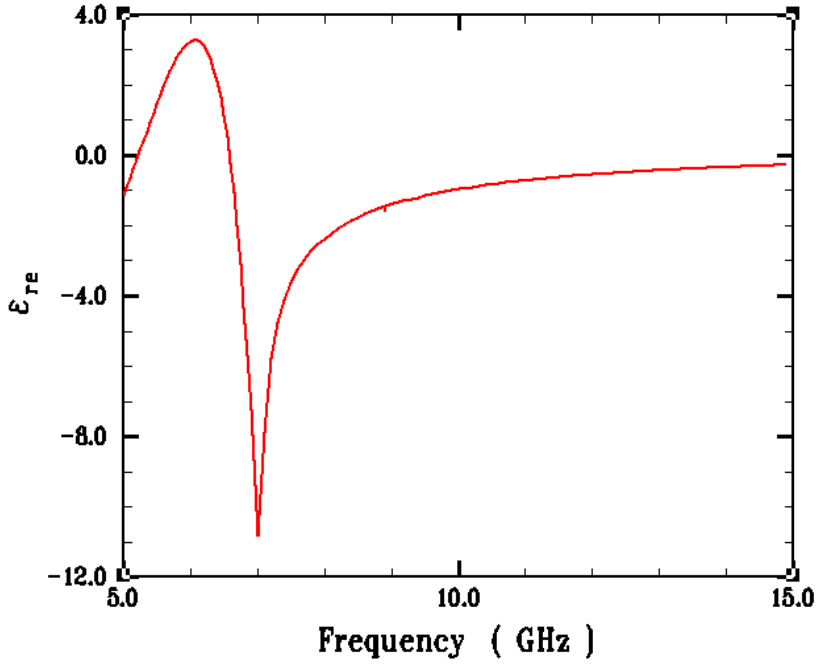


Fig. 15b. Real part of the extracted permittivity values

Figure 15: HFSS-predictions for the CLS-only MTM with the simplified unit cell.

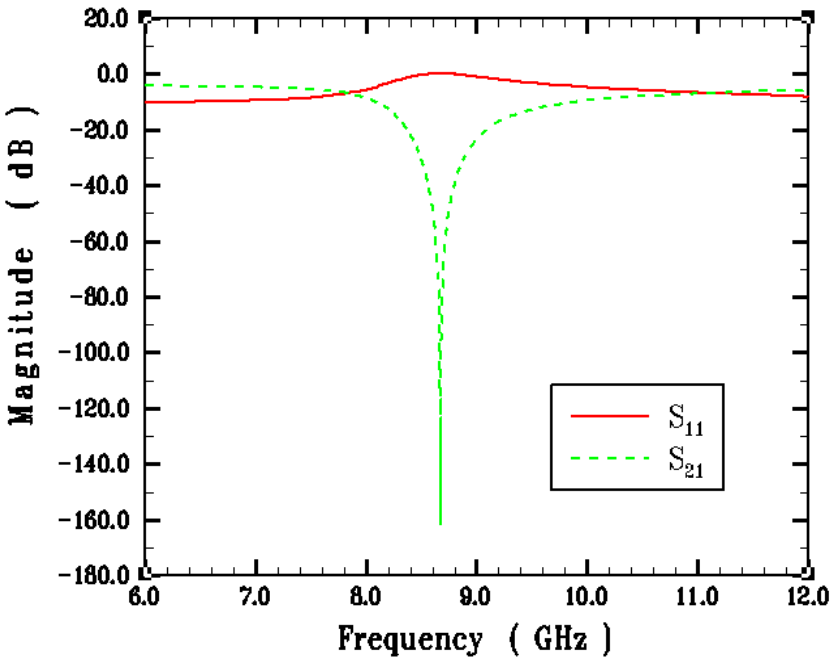


Fig. 16a. Magnitudes of the S-parameters

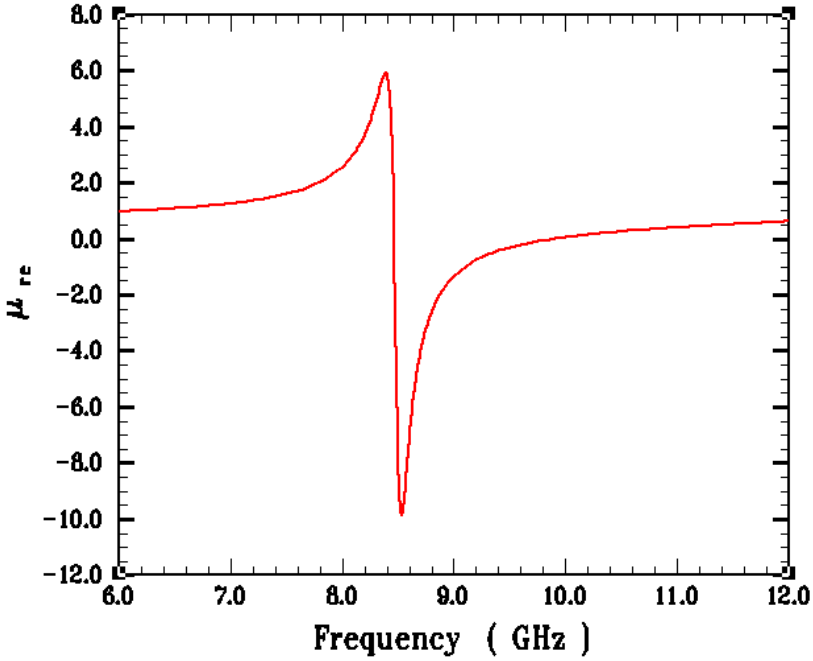


Fig. 16b. Real part of the extracted permeability values

Figure 16: HFSS-predictions for the SRR-only MTM with the simplified unit cell.

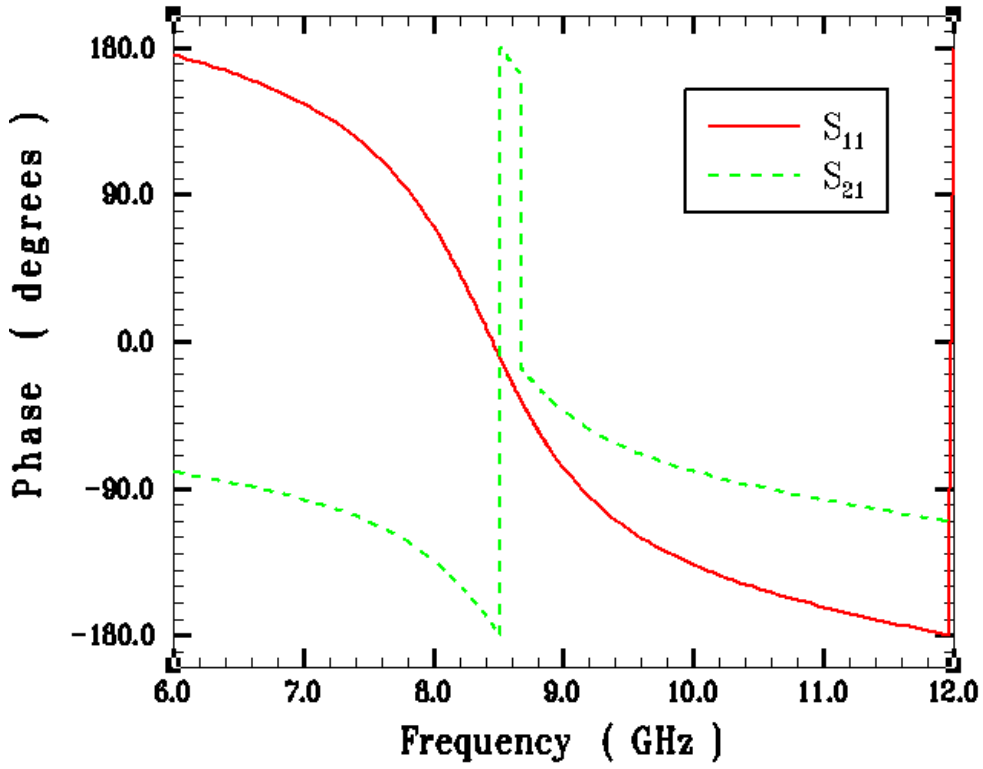


Fig. 16c. Phase of the HFSS-predicted S-parameters for the SRR-only MTM with the simplified unit cell.

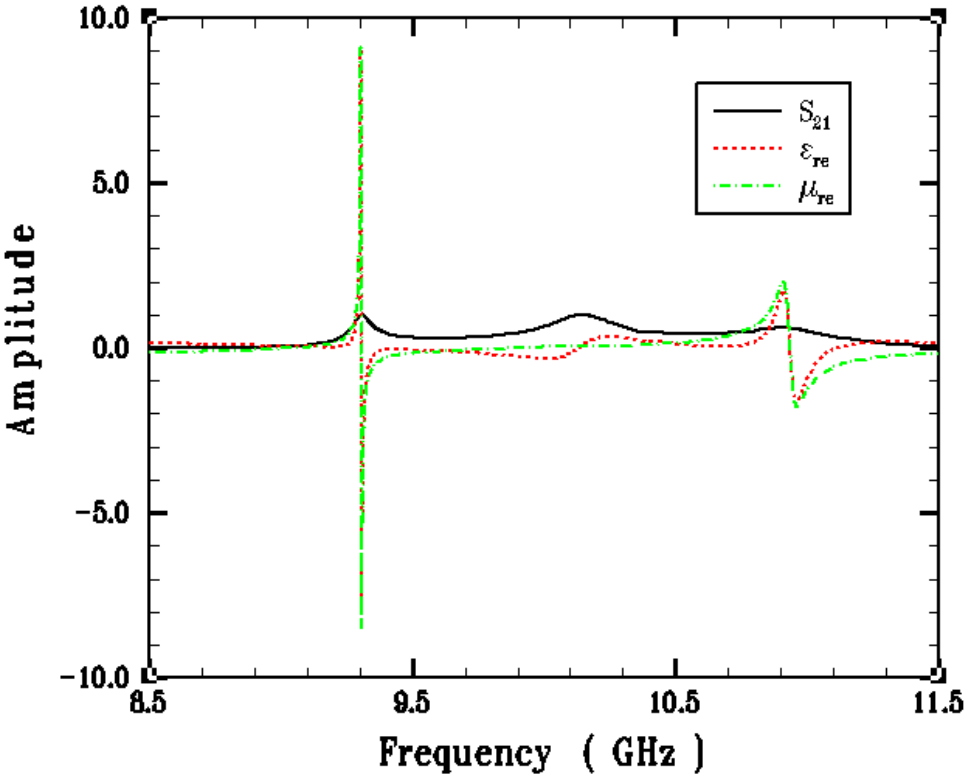


Figure 17: Effective material properties extracted from the HFSS-predicted S-parameters for the complete planar MTM.

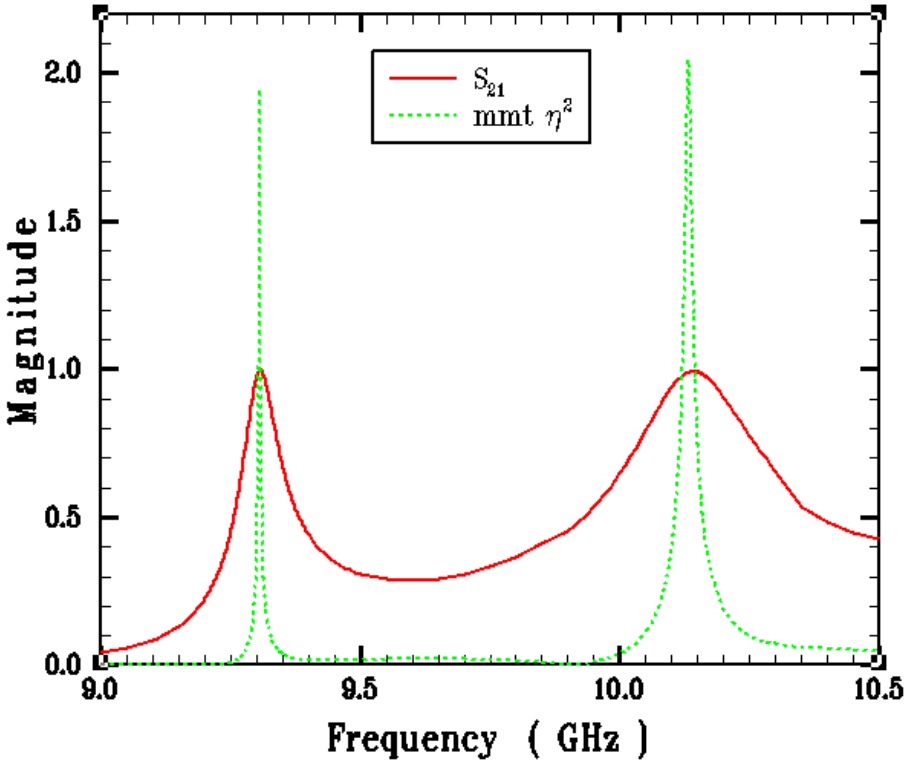


Figure 18: Comparison of the magnitude of the transmission coefficient $S_{21}$ and the impedance term $\eta^2$ extracted from the HFSS-predicted S-parameters for the complete planar MTM.

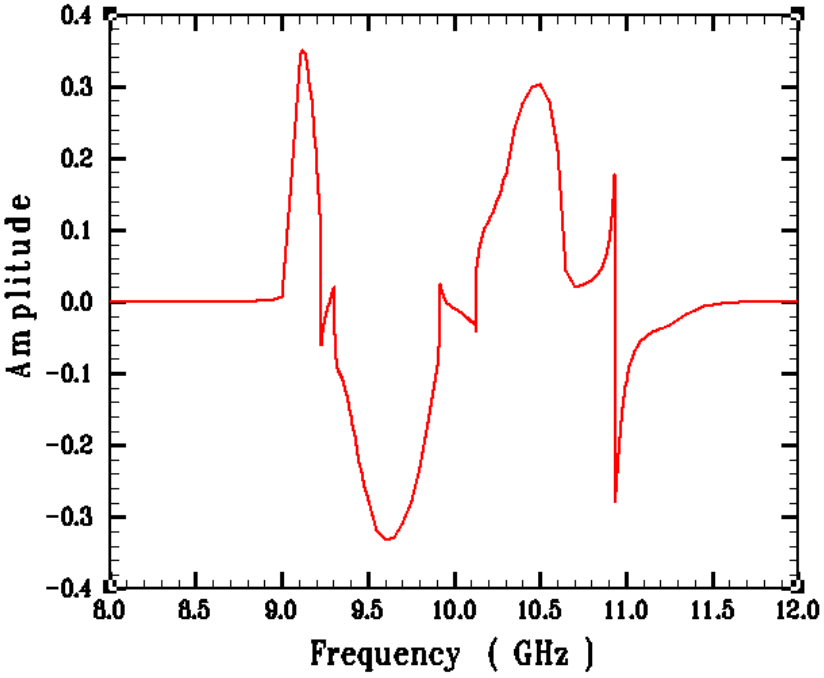


Fig. 19a. HFSS simulation results

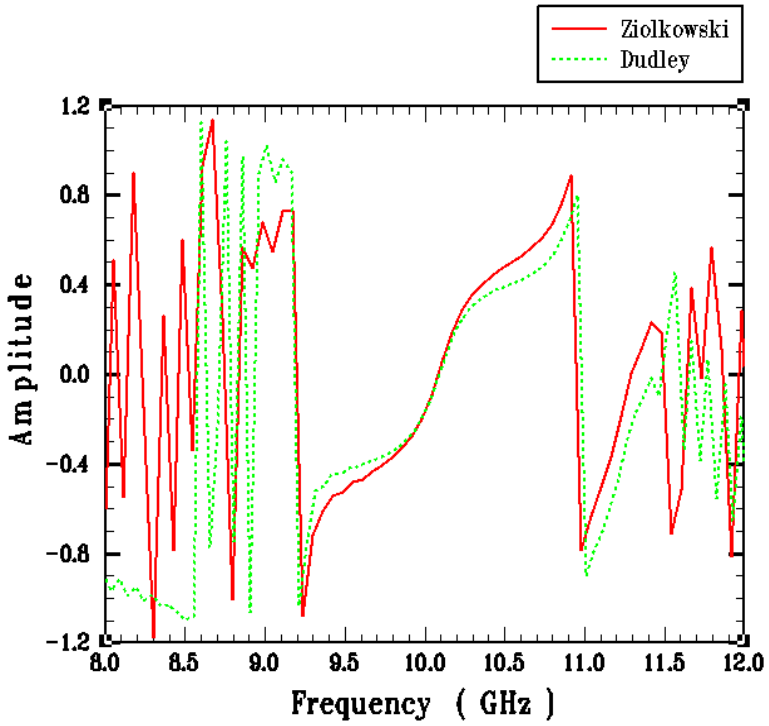


Fig. 19b. FDTD simulation results

Figure 19: HFSS and FDTD predictions of the real part of the index of refraction for the complete planar MTM.